12-2013

Design, Fabrication and Characterization of Plasmonic Fishnet Structures for the Enhancement of Absorption in Thin Film Solar Cells

Sayan Seal
University of Arkansas, Fayetteville

Design, Fabrication and Characterization of Plasmonic Fishnet Structures for the Enhancement of Absorption in Thin Film Solar Cells

Design, Fabrication and Characterization of Plasmonic Fishnet Structures for the Enhancement of Absorption in Thin Film Solar Cells

A thesis submitted in partial fulfillment
of the requirements for the degree of
Master of Science in Electrical Engineering

By

Sayan Seal
University of Calcutta
Bachelor of Science in Physics, 2008
University of Calcutta
Post Bachelor of Science Bachelor of Technology in Radio Physics and Electronics, 2011

December 2013
University of Arkansas

This thesis is approved for recommendation to the Graduate Council.

_____

Dr. Vasundara V. Varadan
Thesis Director

_____ _____

Dr. Hameed Naseem
Committee Member

Dr. Shui-Qing Yu
Committee Member

Abstract

Incorporating plasmonic structures into the back spacer layer of thin film solar cells (TFSCs) is an efficient way to improve their performance. The fishnet structure; which is a tunable, plasmonic light scatterer is used to enhance light absorption. Unlike other plasmonic particles that have been previously suggested, the fishnet is an electrically connected wire mesh and does not result in electric field localization, hence it results in greater absorption in the intrinsic Si layer. Unlike other designs, the fishnet structure is placed in the back spacer layer of the TFSC, so it does not block any incident light. There is also the possibility of integrating back contacts with the fishnet for efficient carrier collection. In addition to its performance, the fishnet structure can be fabricated using low cost nano-imprinting techniques.

The fishnet structure has been studied theoretically in previous research, but this is the first time that the performance of the fishnet has been verified experimentally. The fishnet structure originally proposed in the theoretical study was made of gold, but keeping industrial viability in mind, the choice of metal was changed to silver for this study. The design for the silver fishnet was optimized using full wave electromagnetic simulations in the High Frequency Structure Simulator (HFSS) by Ansoft. The design geometry was tailored to resonate at the band gap of the absorber material (Si), where the absorption coefficient of Si is very low. The goal was to enhance absorption in this region, without causing any degradation of absorption in the other parts of the spectrum.

The silver fishnet structure was fabricated using Electron Beam Lithography (EBL) and thermal evaporation. The other layers of the thin film solar cell (TFSC) were deposited on top of this structure, so that the final fabricated structure optically resembled a TFSC. The absorption of

the sample was measured using Spectroscopic Ellipsometry (SE) and was compared with the absorption of a control sample *sans* the fishnet. It was shown that light absorption is enhanced by a factor of 12.8at the resonance frequency due to the presence of the fishnet structure. The short circuit current (J_{SC}) increased by 30%. Not only was there no observed degradation at other wavelengths, but the overall absorption also increased as a result of using the fishnet.

Even though the fishnet served its purpose of absorption enhancement, there was little correlation between the results of numerical simulations and experimental results. Numerical simulations use values of optical properties from literature as input. These values differ considerably from the materials actually used to fabricate an experimental sample. Also the layer above the fishnet is assumed to be perfectly flat in the numerical model, which is not the case. The 20 nm thickness of the fishnet causes bumps at the AZO –Si interface that must be accounted for given the small thickness of the TFSC layers. The materials used to fabricate the fishnet TFSC were characterized individually using SE. The existence of a bump atop the fishnet was verified using Atomic Force Microscopy (AFM). These factors were included in the theoretical model and the structure was re-simulated to give a much better agreement between theory and experiment.

A fishnet structure in the back spacer layer of a TFSC is proposed to enhance performance efficiency of the TFSC. Nanoimprinting techniques and roll to roll manufacturing can be used to economically fabricate such TFSCs on an industrial scale.

Acknowledgements

I would like to sincerely thank Dr. Vasundara V. Varadan for her invaluable mentorship and support through my MS degree.

I would like to thank Prof. Hameed Naseem and Prof. Shui-Qing Yu for agreeing to serve as part of my committee, and for the guidance and support they have offered throughout.

I would like to thank Prof. J. Cui and Prof. A. Bhattacharyya of the University of Arkansas, Little Rock, for their help and support in our collaborative efforts.

I would like to thank Dr. Mourad Benamara (University of Arkansas) for training me in Scanning Electron Microscopy and Dr. Michael Hawkridge (University of Arkansas) for training me in Atomic Force Microscopy. I would like to thank Mr. Errol Porter (University of Arkansas), for his support during using the equipment at the High density Electronics Center (HiDEC), University of Arkansas.

I would like to appreciate all the help from my colleagues, especially Dr. InKwang Kim, Dr. Liming Ji, and Dr. Vinay Budhraja.

The work in this dissertation is supported by the National Science Foundation under EPS–1003970.

Table of Contents

Chapter 1: Introduction 1

Chapter 2: Background and Motivation 6

2.1 Motivation for Thin Film Solar Cells 6

2.2 Light Trapping in Thin Film Solar Cells 10

Chapter 3: Experimental Details 22

3.1 Design of the Fishnet Structure for a Thin Film Solar Cell 23

3.2 Fabrication of the Thin Film Solar Cell with Fishnet 24

3.3 Measurement of Total Absorption of the Thin Film Solar Cell With and Without the Fishnet Structure 40

3.3(A): Material Characterization 46

3.3(B): Reflection Measurements Using an Ellipsometer 47

3.4 Modification of the Numerical Model and Comparison with Experimental Results 51

Chapter 4: Results and Discussions 53

4.1. Design of the Thin Film Solar cell with a Fishnet Structure in the Back Spacer Layer 53

4.2 Fabrication of the Fishnet Pattern using Electron Beam Lithography 57

4.3 Measurement of Total Absorption of the Fabricated Samples 65

4.4 Ellipsometric Characterization and Structural Modification of Numerical Model 71

4.4.1 Effects of using Ellipsometry-determined Optical Constants in the Numerical Model 72

4.4.2 Structural Modifications in the Numerical Model 77

Chapter 5: Conclusions and Future Work 82

References 84

Appendix 1: License for Figure 2.1 90

List of Figures

Figure 2.1: Price of crystalline silicon photovoltaic cells in $/ watt …...……6

Figure 2.2: Cost breakdowns in wafer solar cell processing……...7

Figure 2.3: Schematic of a typical thin film solar cell…….9

Figure 2.4: Illustration of light trapping using rough surfaces……..12

Figure 2.5: Escape cone defined by the critical angle……...12

Figure 2.6: Nanodome structure for solar cells……..14

Figure 2.7: Electric field enhancement around a gold nanoparticle embedded within SiO_2…….16

Figure 2.8: Fishnet Structure for thin film solar cells……17

Figure 2.9: Absorption co-efficient as a function of wavelength for amorphous silicon……..18

Figure 3.1: Model of the fishnet TFSC constructed in HFSS……23

Figure 3.2: Schematic showing the fabrication process for the fishnet thin film solar cell……...24

Figure 3.3: The JEOL JBX 5500ZD, High Density Electronics Center (HiDEC), University of Arkansas…….26

Figure 3.4: Schematic of spin coating……27

Figure 3.5: Schematic of metal deposition after development……..28

Figure 3.6: Thickness as a function of spin speed for PMMA from MicroChem…….30

Figure 3.7: File conversion in the JEOL JBX 5500ZD…….31

Figure 3.8: Schematic showing the concept of a field……...32

Figure 3.9: Schematic of the JEOL JBX 5500……...33

Figure 3.10: Laser beam controlled sample stage of the JEOL JBX 5500ZD……...36

Figure 3.11: Deflection correction in the JEOL JBX 5500ZD……..37

Figure 3.12 (a) V-VASE system at the University of Arkansas, Fayetteville. (b) Heat stage (c) Rotating stage (d) Focus probes mounted on the source and detector units.....41

Figure 3.13: Beam spot positioned within the fishnet pattern area……42

Figure 3.14 (a) Screenshot of the X-Y alignment process in the WVASE software (b) Screenshot of the Z-alignment process in the WVASE software……44

Figure 3.15: Graph showing accurate fits between measured and fitted calibration data…….45

Figure 3.16: Baseline measurement for ambient light……...47

Figure 3.17: Fit for Ψ and Δ for the standard sample……48

Figure 3.18: Transmission through the fishnet TFSC……...50

Figure 4.1: (a) Total absorption of the TFSC with and without the Fishnet (b) Layer-wise absorption in the TFSC with the Fishnet……...54

Figure 4.2: Electric field in the a-Si layer of the fishnet TFSC computed using HFSS……56

Figure 4.3: SEM pictures for a dose of 1500 μC/cm^2 and a design linewidth of 100 nm (a) Pattern uniform over large area (b) Linewidth of 200 nm obtained on an average……58

Figure 4.4: Using a smaller dose results in underdeveloped pattern…….59

Figure 4.5: Optimization of development time……..60

Figure 4.6: Design linewidth reduced to 85nm, development time reduced to 30 seconds……..61

Figure 4.7: Final dose optimization step……63

Figure 4.8: 100 nm linewidth pattern using a dose of 800 μC/ cm^2, design linewidth of 85 nm, and develop time of 25 seconds…….64

Figure 4.9: Comparison of total absorption with and without fishnet……...66

Figure 4.10: Consistent results for measurements taken for four different samples…….68

Figure 4.11: Measurements consistent for different polarization states……69

Figure 4.12: Comparison between numerical simulation and experimental results (a) With fishnet (b) Without fishnet……70

Figure 4.13: Characterization of the Silicon……..73

Figure 4.14: Characterization of the 100 nm film of silver on silicon substrate……...73

Figure 4.15: Characterization of the 100 nm chromium film on silicon substrate……74

Figure 4.16: Characterization of the 20 nm AZO on silicon substrate……..74

Figure 4.17: Characterization of the 500 nm a-Si on silicon substrate……..75

Figure 4.18: Effect of numerical simulation using optical constants determined from ellipsometry (a) Without fishnet (b) With fishnet……..76

Figure 4.19: Structural modification used in the numerical model (a) Schematic of bump over fishnet (b) Result of AFM measurements taken over the fishnet structure……..79

Figure 4.20: Result of including the bump on top of the fishnet in the numerical model…….80

List of Tables

Table 3.1: Recipe for spin coating……29

Table 3.2: Operating modes of the JEOL JBX 5500ZD……34

Table 4.3: J_{SC} comparison with and without the fishnet structure……67

Chapter 1: Introduction

This thesis deals with the enhancement of efficiency of thin film solar cells. A number of parameters within a thin film solar cell that can lead directly to an increase in efficiency are currently under study. Choice of semiconductor material for the absorber layer (amorphous silicon, cadmium telluride, copper indium gallium diselenide, etc.), high quality contacts, anti-reflection coatings—all of these factors are known to impact the efficiency in a positive way. Incorporating plasmonic structures within the back spacer of thin film solar cells (TFSCs) is yet another efficient way to improve the cell parameters. In this thesis a plasmonic fishnet structure embedded in the back spacer layer of a TFSC is studied. The incorporation of this structure results in an enhancement of light absorption in a-Si, which is used as the absorber material in the thin film solar cell under test.

Thin film silicon solar cells are a better alternative to crystalline silicon solar cells due to numerous advantages like reduced cost, low temperature processing, higher open-circuit voltage and the fact that it can be easily deposited on various substrates without any issues with uniformity. Because of the low minority carrier diffusion length and high recombination rate in the *p* and n layers of TFSCs, the only way to improve the efficiency is to increase the absorption in the amorphous silicon layer. In wafer solar cells, the thickness of silicon is around 180 microns, hence an incoming photon traverses a sufficient path length to get absorbed. In addition, most wafer solar cells use a metallic back reflector that doubles as a back electrode. This doubles the path length of the photon and constitutes one of the simplest light trapping schemes. In thin film solar cells, an enhancement in path length cannot be achieved using such a simple scheme; doubling the path length is far from enough. Rather, a scheme that could scatter

the light within the absorber layer and keep it confined horizontally (waveguide modes) would increase the path length sufficiently, and increase the chance of the photon being absorbed.

There are various techniques used in the processing of TFSCs to enhance the absorption: surface texturing, use of transparent conducting oxide, deposition of amorphous nano-crystalline silicon, etc. Incident light is scattered by the textured surface, and upon reaching the interfaces, the angle of incidence exceeds the critical angle, reflecting the light back into the absorber. This procedure is repeated several times, trapping the light within the absorber layer.

Although these methods are highly cost effective, they do not perform satisfactorily as light trapping designs. Using random surface texturing results in limited absorption enhancement and plateau at an upper limit. Also the surface recombination increases due to rough surfaces. The incorporation of plasmonic nanostructures within the spacer layers also enhances the absorption in TFSCs. The effect of these structures on the performance of TFSC's has been studied experimentally as well as theoretically. But including plasmonic structures made of noble metals has a huge impact on the cost of manufacturing these cells. Therefore unless the advantage of this process is really significant as compared to cheaper alternatives like surface texturing, and economical fabrication methods such as nanoimprinting can be developed, it may not mature into a viable industrial practice.

Metal nanoparticles enclosed within a dielectric absorb incident photons at specific wavelengths depending upon their size. The absorbed photons are radiated diffusely, and the scattering pattern depends on the geometry of the plasmonic structure. This also gives us the same scattering effect as surface texturing, but with several advantages. The size of nanoparticles is much smaller, and more importantly, the scattering can be tailored to occur at a specific

frequency. The material, geometry, and layout of these particles define the frequency at which they will absorb photons, and subsequently radiate.

Many research groups have reported an increase in absorption in plasmonic solar cells using metallic nanoparticles arrays in the front spacer layer. Although there is significant enhancement, a lot of light is also lost due to shadowing. It has also been demonstrated that using plasmonic structures at the back spacer is a better alternative, especially when the enhancement has to be targeted at longer wavelengths which uses larger nanoparticles (Ji and Varadan).

Despite the reported enhancement achieved by nanoparticles, one fact still remains—due to the high electric field localization around the nanoparticles, the loss is very high. The reason for this localization is that the nanoparticles are electrically isolated. A scheme whereby these particles could be electrically interconnected could solve this issue.

The plasmonic fishnet structure is one such geometry by which this effect can be realized. As its name suggests, it is a two dimensional net made of a thin film of metal. The ability of this structure to enhance the absorption and short-circuit current density in thin film solar cells has already been established theoretically through numerical simulations (Ji and Varadan). In accordance with this design a plasmonic fishnet was embedded within the back spacer layer of a thin film solar cell structure. The incoming light is scattered into the absorber layer and trapped by total internal reflection from the top interface of the absorber layer. This increases the effective path length of the photon within the absorber material and increases the probability of the photon being absorbed and converted into an electron-hole pair. So despite being a very thin film, the absorber seems to be much thicker in effect.

The fishnet is inherently different from a regular scatterer; the frequency of operation can be tuned in the fishnet. The linewidth, pitch size, thickness and choice of material define the plasmonic resonant frequency of this structure. For this specific case, the fishnet was designed to provide a plasmonic resonance at the bandgap of a-Si, which corresponds to a wavelength of around 680 nm. The absorption of a-Si is very weak in this region. Silver was used to make the fishnet structure, and the design was optimized using full wave electromagnetic simulations in the High Frequency Structure Simulator (HFSS) by Ansoft.

The fishnet structure made of silver was fabricated using electron beam lithography and thermal evaporation. The final fabricated structure optically resembled a TFSC. The results predicted by numerical simulations were reproduced experimentally on a fabricated sample. The reflection from the sample was measured using spectroscopic ellipsometry, and the absorption in the absorber layer was computed from these measurements. The results were compared with a thin film solar cell without the fishnet and it was found that the absorption was enhanced by a factor of 12.8 at the resonance frequency. In fact, there was an increase in the overall absorption across the entire wavelength range as well. With plasmonic structures made of noble metals, it is always a matter of concern whether the trapped energy is being successfully absorbed. It could also be expended as loss in the metal. It was shown that in this case, 83% of the absorbed power was absorbed successfully by the absorber layer. The structure intensifies the electric field within the absorber layer, with marginal loss in the metal.

When the results of the experiment were compared with the results predicted by numerical simulations, it was found that the agreement was poor. This was a matter of concern because it introduced a large degree of uncertainty while predicting how these structures

behaved. Upon further investigation, it was found that the material properties as well the surface morphology of the thin film solar cell under test were described inaccurately by the existing model. After appropriate modifications were made, the agreement between theory and experiment showed good agreement.

In this thesis, a complete account of fabricating a plasmonic design for a thin film solar cell has been discussed. An existing design was modified to offer a low cost alternative. A full fabrication process for the design has been developed and reiterated several times to check for repeatability. Although the EBL process is very slow for processing these cells on a commercial scale, nanoimprinting facilities can be used to produce them as part of an assembly line. When all these cells were tested optically for absorption, it was found that the absorption was enhanced as a result of including the fishnet. As a conclusion to this study, the experimental results were used to improve the numerical model, which will aid in the engineering of similar structures in the future.

Chapter 2: Background and Motivation

2.1 Motivation for Thin Film Solar Cells

The cost per watt of solar cell technology has been on the decline since its inception. Figure 2.1 shows that the cost per watt of a crystalline silicon solar cell module today is less than one hundredth of its cost in 1977 [1]. The question, however, is that is this enough to make solar energy a viable option in the future? The short answer is no. Despite falling prices, solar energy is still far more expensive than other options available in renewable energy: like wind, hydro-electricity, biomass, and geothermal [2]. Unless steps are taken to bring this cost down, there is little chance that solar cells will see the light of day as a viable source of clean energy.

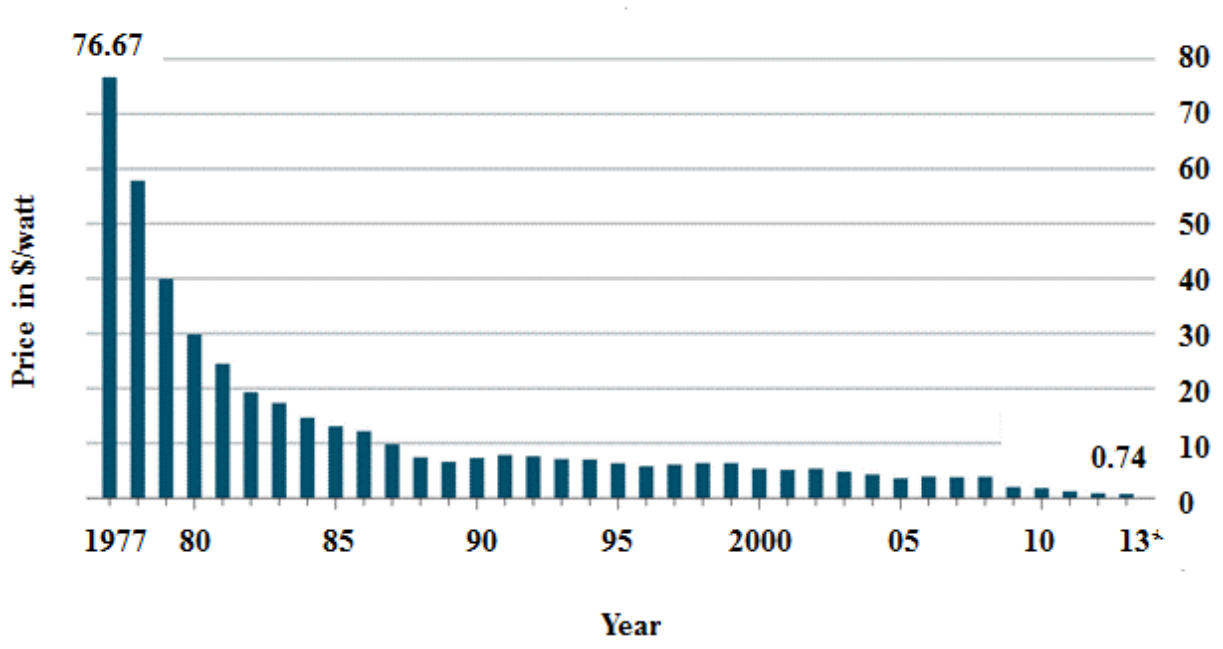

Figure 2.1: Price of crystalline silicon photovoltaic cells in $/ watt [1]

Figure 2.2 gives the cost breakdown in the manufacture of a wafer solar cell [3, 4]. It can be seen that the 67% of the cost is that of the wafer itself, with 22% of the cost incurred by the metallization process. Hence if the cost in the two aforementioned areas can be reduced significantly, the overall cost of production will also decrease significantly. This is the point at which Thin Film Solar Cells (TFSCs) assume importance.

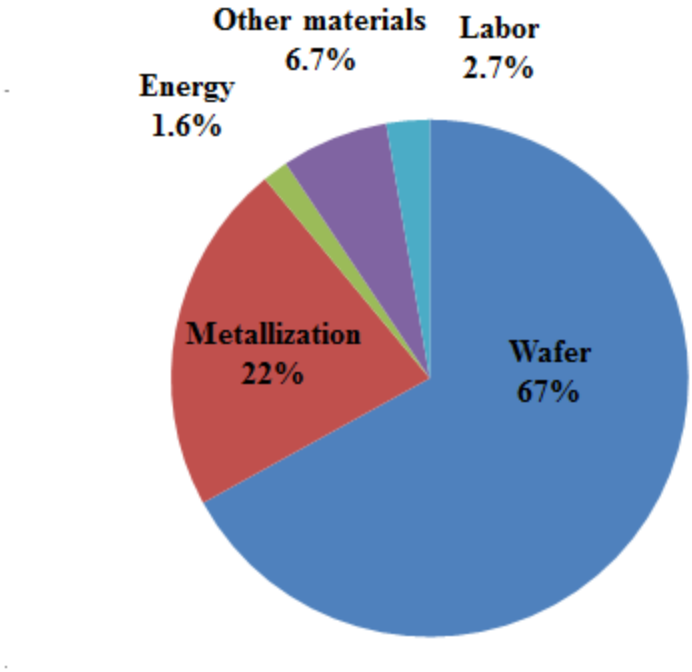

Figure 2.2 Cost breakdowns in wafer solar cell processing

Thin film solar cells are the way forward for the solar cell industry. Thin film solar cells use 90% less material as compared to conventional wafer solar cells. This drastically reduces the cost of manufacturing thin film solar cell modules. They have numerous other advantages—low

cost processing, easy deposition methods and less raw material requirement. A detailed discussion on the impact of thin film silicon solar cells was given by A. Shah et al, 1999 [5]. The possibility of cutting costs by employing roll-to-roll manufacture methods was also discussed.

Fig. 2.2 shows a simple schematic of a typical TFSC. The substrate used is typically glass, with a back electrode made of a thin film of metal (silver, gold, aluminum, copper, etc.). Above this layer there is a back spacer layer made of a transparent conductive oxide like Indium Tin Oxide (ITO) or Aluminum-doped Zinc Oxide (AZO). Following this, we have the semiconductor layer that actually absorbs photons and generates an electron-hole pair. The choice of material for this layer ranges from amorphous Silicon (a-Si), to Cadmium Telluride (CdTe), to the more recently developed Copper Indium Gallium Diselenide (CIGS) and CZTS cells. Amorphous silicon is still one of the most widely used materials today, although CIGS cells have been reported to have the highest efficiency of 19.2% [6], or more recently 20.3% [7]. One of the major reasons for this could be the toxicity of Cadmium [8-10]. Amorphous silicon is abundant, non-toxic, and can be processed at relatively lower temperatures [11-13]. Thin films of amorphous silicon also show minimum light induced degradation (the Staebler-Wronski effect) [14, 15]. The a-Si layer is usually a p-i-n junction, but the optical properties of p-, i- and n- type a-Si are essentially the same. Hence from an optical viewpoint, they can be lumped into a single absorber layer as shown in Figure 2.3.

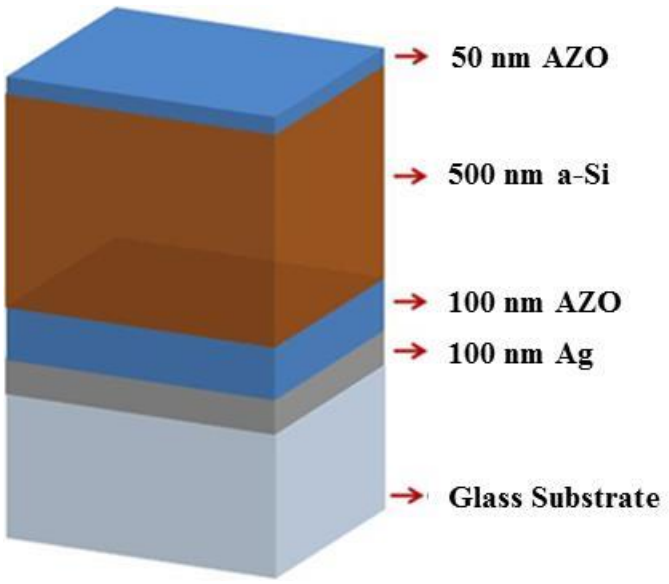

Figure 2.3 Schematic of a typical thin film solar cell

The efficiency values reported for CIGS cells are very high for thin film cells, but they do not match up to the high efficiencies recorded for crystalline silicon cells. As of June 2013, SHARP has reported the highest efficiency for an InGaAs triple junction concentrator cell at 44.4% [16], more than double that achieved by a thin film cell. Note that these record cells have very complicated design specifications that may not be practical to manufacture on a commercial scale. The efficiencies of commercial modules built based on these designs are typically much lower.

The high efficiencies for wafer solar cells come at a very high cost per watt, as already mentioned. This where thin film solar cells can be competitive, since they cost only a fraction of the high efficiency crystalline solar cells. However, the efficiency of existing thin film solar cells needs to be enhanced considerably to compete with wafer solar cells. To a great extent, this can

be achieved by a combination of two methods—engineering high quality materials for the absorber layer and devising efficient light trapping techniques [17].

2.2 Light Trapping in Thin Film Solar Cells

The typical thickness of an a-Si thin film solar cell is 500 nm. This is because the diffusion length of carriers in a-Si is around 400 nm [18]. This is very little material as compared to conventional wafer solar cells, which are typically made from 180 μm thick wafers to ensure sufficient light absorption [19]. Thus, in wafer solar cells, an incoming photon covers a large enough path length within the absorber material to be absorbed successfully. In thin film cells, on the other hand, due to reduced thickness, the path length of the incoming photon has to be increased to ensure successful absorption. Otherwise the probability of the photon being absorbed is reduced greatly. This could be made possible if there was some way in which we could trap the photon within the thin film absorber layer. This would increase the effective path length of the photon within the material, thereby increasing its probability of being absorbed. The process of manipulating the incoming light to confine it within the absorber layer is known as light trapping.

The schematic in Figure 2.4 (a) shows the case of a thin film solar cell in which a metallic back reflector has been incorporated. This back reflector doubles as a back electrode for carrier collection [20]. This is the simplest form of light trapping that doubles the path length of the incoming light beam through the absorber material. Light entering the solar cell will experience specular reflection at the metallic back electrode and exit the cell through the top

surface. This gives a normally incident photon a path length of approximately a micron to get absorbed. However, this path length is still not enough to ensure that the photon will in fact be absorbed. For example, let us consider a thin film solar cell using amorphous silicon as the absorber. The absorption co-efficient α of amorphous silicon is 7.9×10^4 cm^{-1} at a wavelength of 588 nm. According to the Beer-Lambert law [21] in one dimension,

$$I = I_0 \exp(-\alpha x)\,\mathrm{cm}^{-1} \quad \ldots(2.1)$$

Here I_0 is the incident light intensity and I is the light intensity after traversing a distance x within the material. The intensity, in turn, is a measure of the number of photons per unit area per unit time. From Eq. (3.1) it can be easily calculated that for a beam of light of wavelength 588 nm incident normally on the top surface a 500 nm amorphous silicon thin film, nearly 50% of the incident photons do not get absorbed. This means that we will be getting very little voltage output from a thin film solar cell if such a rudimentary light trapping method is employed. We need a more efficient light trapping scheme that enhances the cell performance, without degrading carrier transport.

Figure 2.4 (b) shows a thin film solar cell in which a common light trapping method is employed. In this cell, the back spacer layer has a random rough surface. Although this method is only suitable for wafer cells, it serves well to illustrate the principle of light trapping. When a beam of light is normally incident on the top surface of this cell, it gets reflected diffusely in all directions. On reaching the top surface, all the reflected beams striking the top spacer-amorphous silicon interface at an angle greater than the critical angle θ_c, will be reflected back into the absorber layer. This process will repeat itself and light trapping will be achieved. There exists an

escape cone defined by θ_c, within which all reflected rays will escape from the top surface (Figure 2.6). This escape cone should cover minimum volume for a good light trapping design.

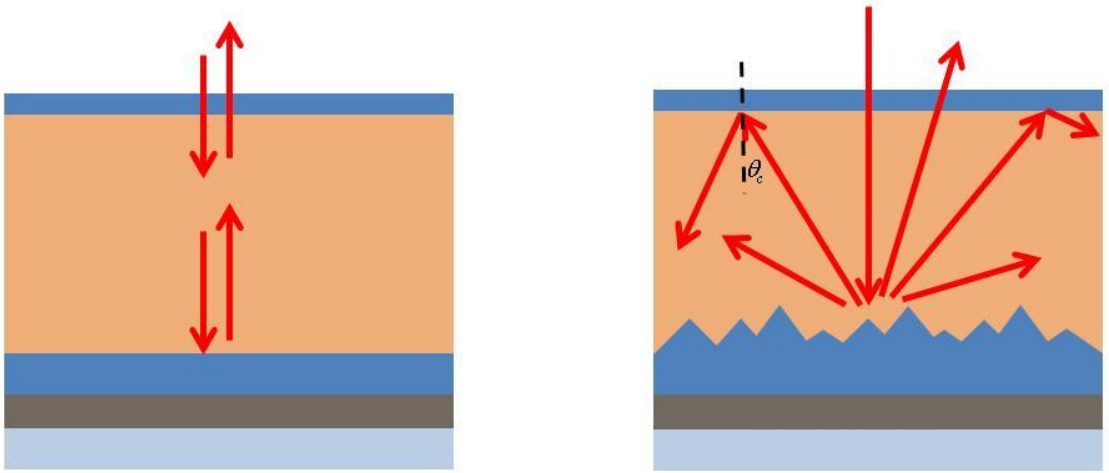

(a) Simple light trapping scheme (b) Light trapping using rough surfaces

Figure 2.4: Illustration of light trapping using rough surfaces

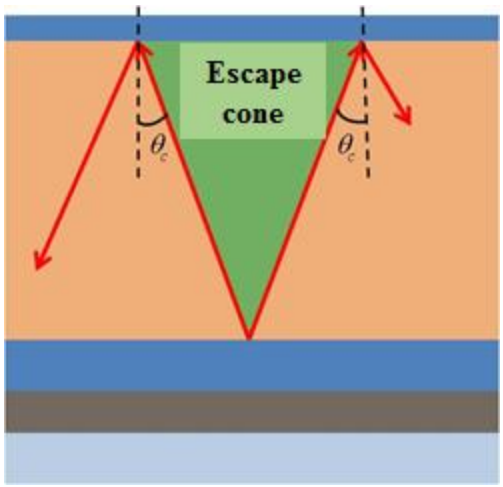

Figure 2.5: Escape cone defined by the critical angle

This concept has been studied in great detail theoretically in the past [22, 23]. Calculations show that the maximum enhancement that can be achieved by a random rough surface is $4n^2$, where n is the refractive index of the absorber material. Of course if we take into account that the top of the absorber surface is coated with an transparent conductive oxide (TCO) layer for surface passivation and anti-reflection, this limit further reduces to $4n^2/n_s^2$, where $n_s$is the refractive index of the TCO layer [24]. Also, the typical roughness used for light trapping purposes is of the order of 5 μm. This makes the above technique strictly applicable to thick wafer solar cells only.

The same concept was also extended to thin film solar cells by using the Asahi U-type substrate [25-28], where a substrate with a surface roughness of about 40 nm is used. The degree of scattering achieved by this substrate can be quantified by a parameter known as haze factor. The haze factor for the Asahi U-type process is only 10% [25]. More advanced processes like the Asahi HU-type process have a haze factor as high as 90% [25], but it has also been established that for a haze factor beyond 40%, the quantum efficiency and short circuit current density saturates, yielding no further enhancement [29]. A lot of work has also been reported where thin film cells deposited on textured ZnO have been shown to perform at par with the Asahi U-type substrate [30-33]. Further, the enhancement also saturates beyond a surface roughness of 35 nm for the Asahi substrate [25].

It was recently demonstrated by S. Fan et al, that for random photonic structures in thin film solar cells, the absorption enhancement could exceed the $4n^2$ limit [34] that curtails the enhancement in wafer cells. Instead of random rough surfaces, nanophotonic structures like the nanodome geometry have been proposed by S. Fan et al [35] and S. J. Fonash et al [36]. These

designs showed a maximum of 53% increase in the short circuit current density as compared to a planar cell [36]. Figure 2.7 shows a schematic for the nanodome solar cell.

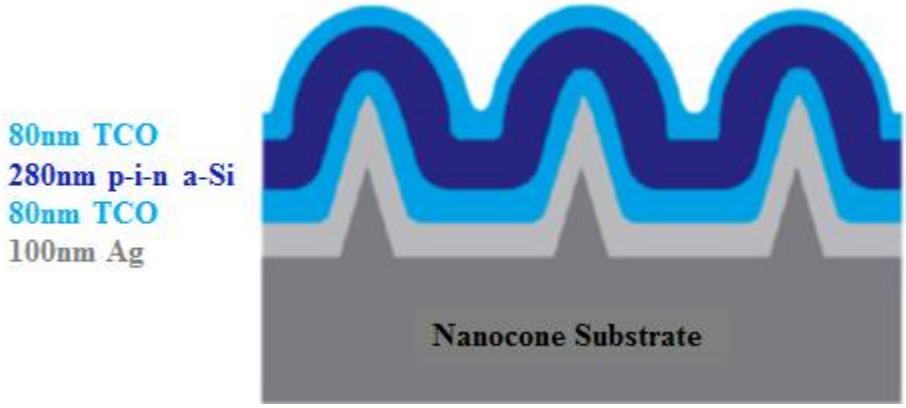

Figure 2.6: Nanodome structure for solar cells [36]

Shaping the back spacer layer in the form of blazed gratings was illustrated by Heine and Morf [37], which resulted in an increase in reflectivity by a factor of 5. Similar schemes have also been proposed by S. Ruby et al [38], and grating couplers for solar cells have been proposed by Haase and Steibig [39]. The major drawback of these schemes is the fact that they result in thicker devices with a greater possibility of surface recombination by creating defects within the semiconductor material. This compromises the photovoltaic capability of the material [40-42], and is opposed to the idea of moving to thin film solar cells in the first place. Instead a planar structure would be more preferable which contributes minimally to the thickness of the device, while providing a significant enhancement in performance.

Other low-cost solutions for absorption enhancement involve front surface anti-reflection coatings using nanostructure arrays [43-45]. D. Lehr *et al* proposed a number of geometries in

their comparative study of front surface nanostructure arrays [43]. Conical and Gaussian irregularities were studied and it was demonstrated that the profile of the periodic structures defined the performance of the coating at the long wavelength region. P. Barry *et al* proposed a nanodome-like front surface layer [45], and reported an enhancement factor of 119, well above the corresponding Yablonovitch limit of 50. The deposition of nanoparticles on the front surface and utilizing the plasmonic effect [46-52]. Structures exhibiting plasmonic effect are typically nanoparticles of noble metals, like gold and silver, or even aluminum, that are embedded within the front spacer layer using inexpensive fabrication techniques.

When light is incident on metal-dielectric interface, collective oscillations of electrons known as surface plasmons are excited. However, this excitation occurs only at certain frequencies known as the plasmonic resonance frequency and is unique. The surface plasmons absorb photons at the resonance frequency, which manifests itself as a decrease in reflection (or increase in transmission) from (through) these structures [53-55].

To generate plasmons with light, the momentum has to be matched [56] and this can be done using prism coupling [57], sub-wavelength features like nanopores [58], or periodic diffraction gratings on the metal surface [59,60].

Instead of a thin metal film on a dielectric material, if we have a suspension of metal nanoparticles, then the surface plasmons will not propagate but will resonate and remain localized. The curved surface of the nanoparticle exerts a strong restoring force on the electron wave. This leads to resonance and a strong enhancement of the incident field in the near-field of the metal nanoparticle. Figure 2.7 shows an electric field plot showing the concentration of the electric field around a gold nanoparticles, 40 nm in diameter and embedded within SiO_2.

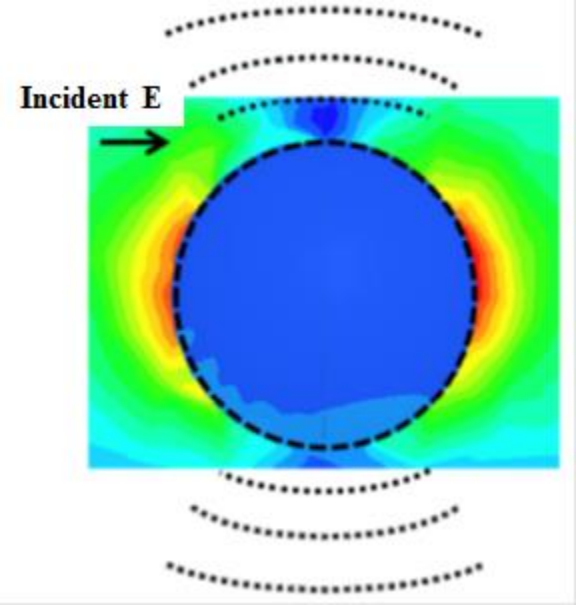

Figure 2.7: Electric field enhancement around a gold nanoparticle embedded within SiO_2 [24]

The frequency of resonance is different for different materials. For gold and silver, the Plasmon resonance frequency lies in the visible range. Once the plasmons absorb the incident photon, they release the absorbed energy in the form of a photon as well; but the directon of radiation depends on the properties of the metal and dielectric, as well as the geometry of the metal nanostructure. The nature of radiation is similar to electric dipole radiation [24]. Hence the plasmonic structure acts as a frequency tuned scatterer. When plasmonic structures are incorporated within the back spacer layer of thin film solar cells, this scattering phenomenon gives rise to light trapping, as explained previously. However this time, the light scatterer can be confined to much thinner geometries and contributes minimally to the thickness of the solar cell.

The plasmonic fishnet structure has already been proposed and studied theoretically by L. Ji and V. Varadan [61]. This design was based on negative index metamaterials for microwave

applications by S. Zhang et al [62, 63] and V. Varadan *et al* [64]. The resonance frequency of these structures could be tuned depending upon the line width, thickness, spacing, and material properties. Initially, common microwave metamaterials like split ring resonators were proposed by V. Varadan and L. Ji [65] for use in the back spacer of thin film solar cells as plasmonic scatterers. However, it was demonstrated by L. Ji that electrically isolated plasmonic structures had significant losses associated with electric field concentration around these structures [24, 65]. Hence, the fishnet structure was proposed, which operates as an LC oscillator (similar to the split ring resonator), but provides electrical connectivity to reduce losses.

Figure 2.8 (a) shows the schematic of the fishnet structure and Figure 2.8 (b) shows how this structure was incorporated within the solar cell.

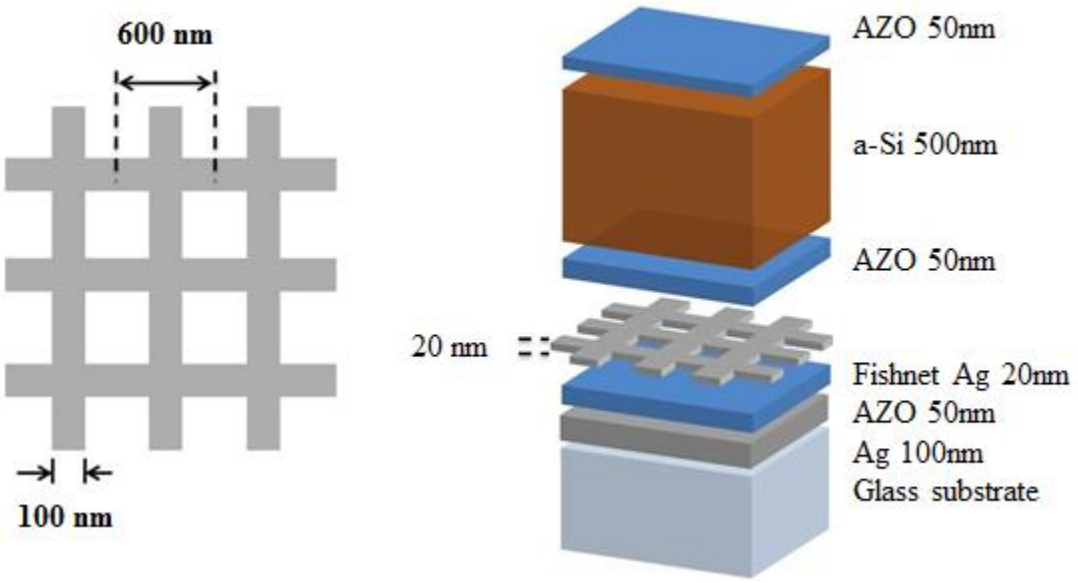

(a) Schematic of the Fishnet Structure

(b) Schematic of the Fishnet TFSC

Figure 2.8: Fishnet Structure for thin film solar cells

The fishnet structure was designed to provide a plasmonic resonance at a wavelength of around 680 nm, which is the band gap of a-Si. The absorption of a-Si is very low at this region (Figure 2.9). Boosting the light absorption around this wavelength will also improve the electrical output from the solar cell. In addition to this there is also the possibility of integrating contacts to the fishnet for more efficient carrier collection.

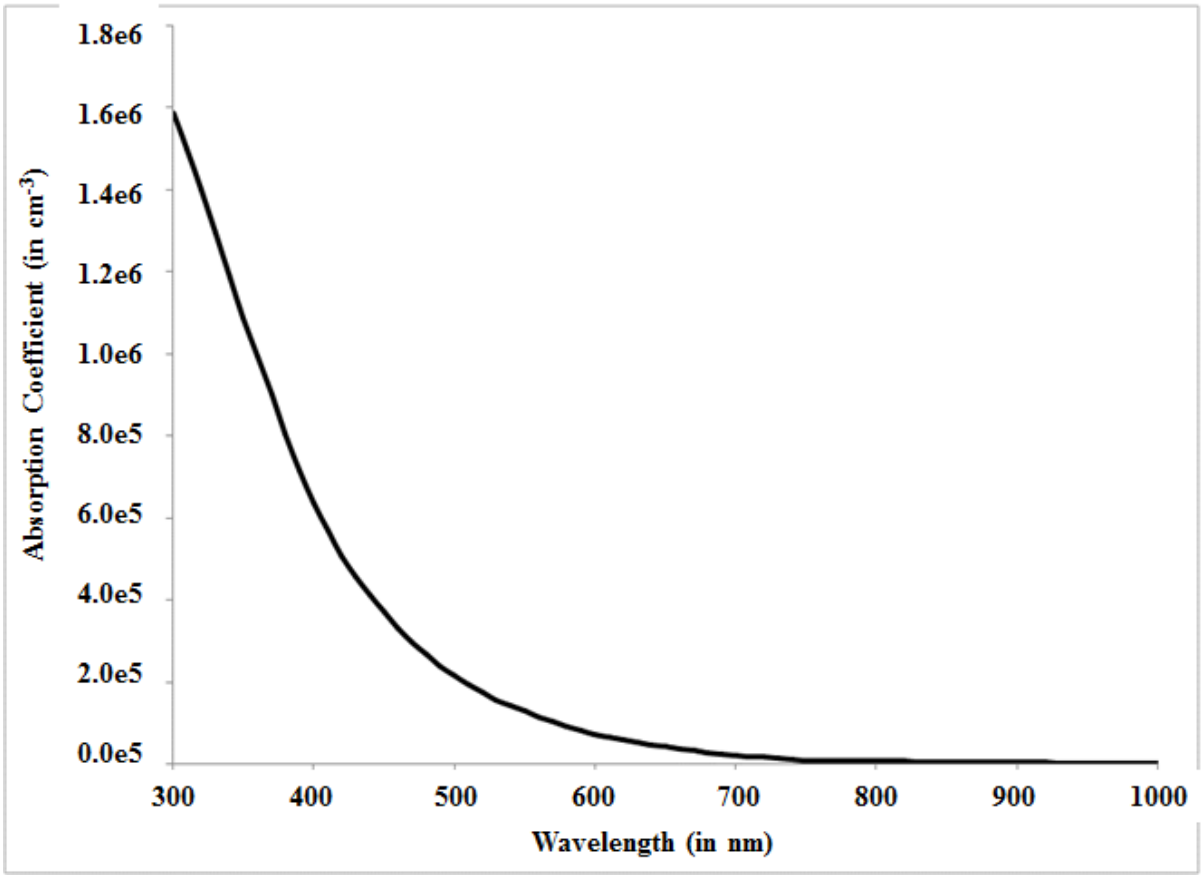

Figure 2.9: Absorption co-efficient as a function of wavelength for amorphous silicon

Using plasmonic structures in the front spacer of thin film solar cells is usually more common. Atwater et al [52, 66-69] have proposed several such nanoparticles arrays that cause an improvement in performance of thin film solar cells. Also, using nanoparticles at the front end was shown to reduce the sheet resistance, resulting in an increase in the fill factor [52]. They have also proposed using plasmonic structures at the back spacer [66] and have verified that they are more effective than using randomly textured or planar back contacts. Other notable contributions include work by S. Fan *et al* [70] who proposed similar front end metallic gratings that showed up to 50% enhancement in absorption. Instead of randomly distributed particles, periodic structures are also commonly used for plasmonic designs. More recently in 2013, R. Pala (from H. Atwater's group), S. Fan and M. Brongersma, along with other members of their group, proposed a semi-analytical model in which they investigated the effect of using non-periodic schemes instead of conventional periodic gratings [71]. These structures were pseudo-random, and the varying periodicity is based on the Fibonacci and Rudin-Shapiro sequences. It has been shown that such non-periodic schemes in some cases these patterns are better suited to cause enhancement as compared to completely random or completely periodic sequences.

M. A. Green et al proposed plasmonic nanoparticle based solar cells and reported a 16 fold enhancement in absorption for silicon on insulator solar cells [48]. They also studied the effect of varying particle size on the absorption. It was demonstrated that for red shifting particle resonances, larger particles were required. This exposes a major drawback of front surface plasmonic designs. For enhancement at longer wavelengths, larger particle sizes will obstruct incoming light.

With regard to front surface plasmonics blocking the path of incoming light, evidence was provided by Brongersma et al who demonstrated an enhancement in the absorption using periodically spaced metal strips on the front end of thin film solar cells [71]. In this study, broadband enhancement was achieved. However, when the critical dimension of the metal strips exceeded 100 nm, the strips acted like reflectors, thus preventing light from entering the cell. Best results were achieved using strips that were 50 nm – 100 nm wide.

Research efforts are gradually focusing on moving plasmonic structures to the back spacer layer in thin film solar cells. The most recent effort that comes to mind is a study by Miro Zeman *et al* in 2012 [72] where they have argued that front surface plasmonics tend to suppress the photocurrent below the surface plasmon resonance. They used randomly distributed silver nanoparticles between 5 nm and 35 nm in diameter. The performance of the structure of comparable to conventional textured back reflectors, but do not risk the degradation of semiconductor material, which is the case for texturing [40-42].

The above studies prove conclusively that plasmonics greatly enhance light trapping in thin film solar. More importantly, the designs are simple and easy to fabricate commercially. However, the designs discussed above are front surface designs. Although there is an enhancement in absorption, part of the incoming light is blocked by the nanoparticles. Further, for boosting absorption at longer wavelengths, comparatively larger nanoparticles are required [24]. This only serves to worsen the shadowing problem. So, the full capability of plasmonic enhancement cannot be tapped using front surface designs.

A fishnet design on the front of a thin film solar cell will also be an effective plasmonic scatterer, but it will not work as well as a back spacer fishnet [24]. Also there is very little work

that has been done in connected structures like the fishnet. The electrical connectivity of this structure serves to minimize losses associated with the metal.

Chapter 3: Experimental Details

In this chapter the details relevant to the experiment will be presented. This will include a detailed description of the equipment used, and an account of how each of the equipment was used to achieve the final results. This project can be broadly classified into three major sections,

(1) Design of the thin film solar cell with the fishnet: This was done using the High Frequency Structure Simulator (HFSS) by *Ansoft*. A brief overview of the design and simulation process using HFSS will be presented in Section 3.1.

(2) Fabrication of the thin film solar with the fishnet in the back spacer: The thin film layers were deposited using a variety of techniques like thermal evaporation, plasma enhanced chemical vapor deposition (PECVD), and DC sputtering. However, the major challenge in the fabrication process was the fabrication of the fishnet structure. This was done using electron beam lithography; hence this technique will be discussed in great detail in Section 3.2. This discussion will include the details of the process, right from the spin coating of electron sensitive resist to lifting off the excess metal to obtain the fishnet structure.

(3) Measurement of total absorption of the thin film solar with and without the fishnet: The final step was the measurement of the total absorption with and without the fishnet structure, and hence verify experimentally whether there was any enhancement as a result of using the fishnet structure. The measurement was done using a spectroscopic ellipsometer. In addition, the ellipsometer was used to characterize the materials used to fabricate the thin film solar cell to obtain a better fit between theoretical and experimental results. A detailed description of the instrument as well the experimental technique will be provided in Section 3.3.

3.1 Design of the Fishnet Structure for a Thin Film Solar Cell

The design for the fishnet solar cell was simulated using HFSS by Ansoft. It is a 3D full wave electromagnetic simulation tool. Figure 3.1 shows the model of a unit cell of the fishnet solar cell constructed in HFSS and points out the design specifications and ports. Master-slave boundary conditions were used since the structure was periodic.

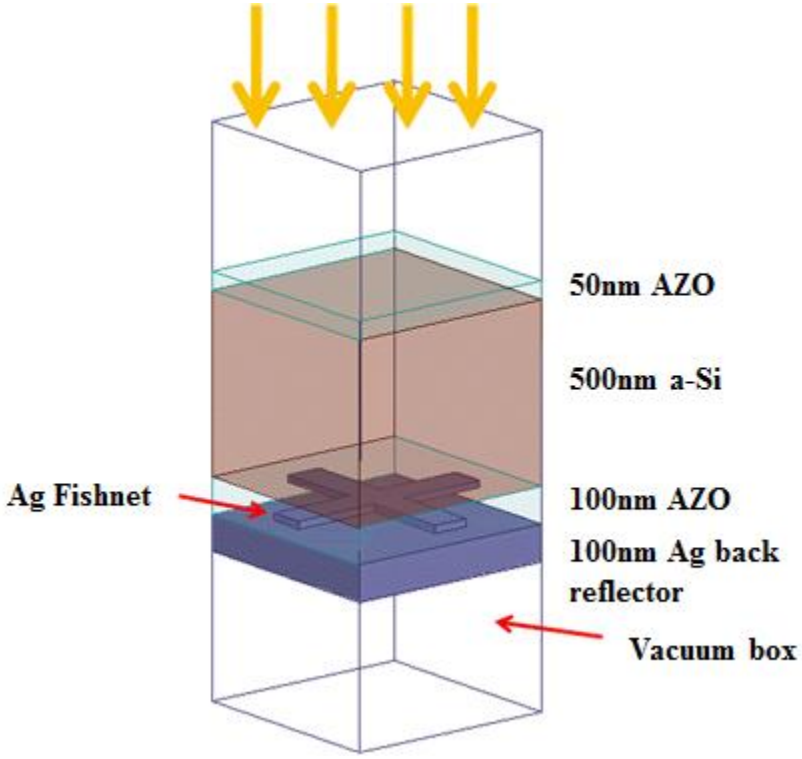

Figure 3.1: Model of the fishnet TFSC constructed in HFSS

The material constants used for simulation have been taken from well cited sources [73, 74]. The number of modes that were solved was 10. All the modes with non-zero attenuation have to be included to get an accurate simulation. The simulation was done for the wavelength range 400 tHz to 750 tHz, in steps of 10 tHz. Modifications were made to the model to obtain a better match between simulation results and measured data, but they will be discussed in due

course. The ports and simulation parameters were kept the same, only the material properties were changed and a few features were added.

3.2 Fabrication of the Thin Film Solar Cell with Fishnet

A large component of this thesis deals with the fabrication of the fishnet solar cell. Before discussing any of the methods undertaken, it is very important to present a brief overview of the fabrication process. Figure 3.2 shows a schematic that outlines the various steps required to fabricate a fishnet solar cell.

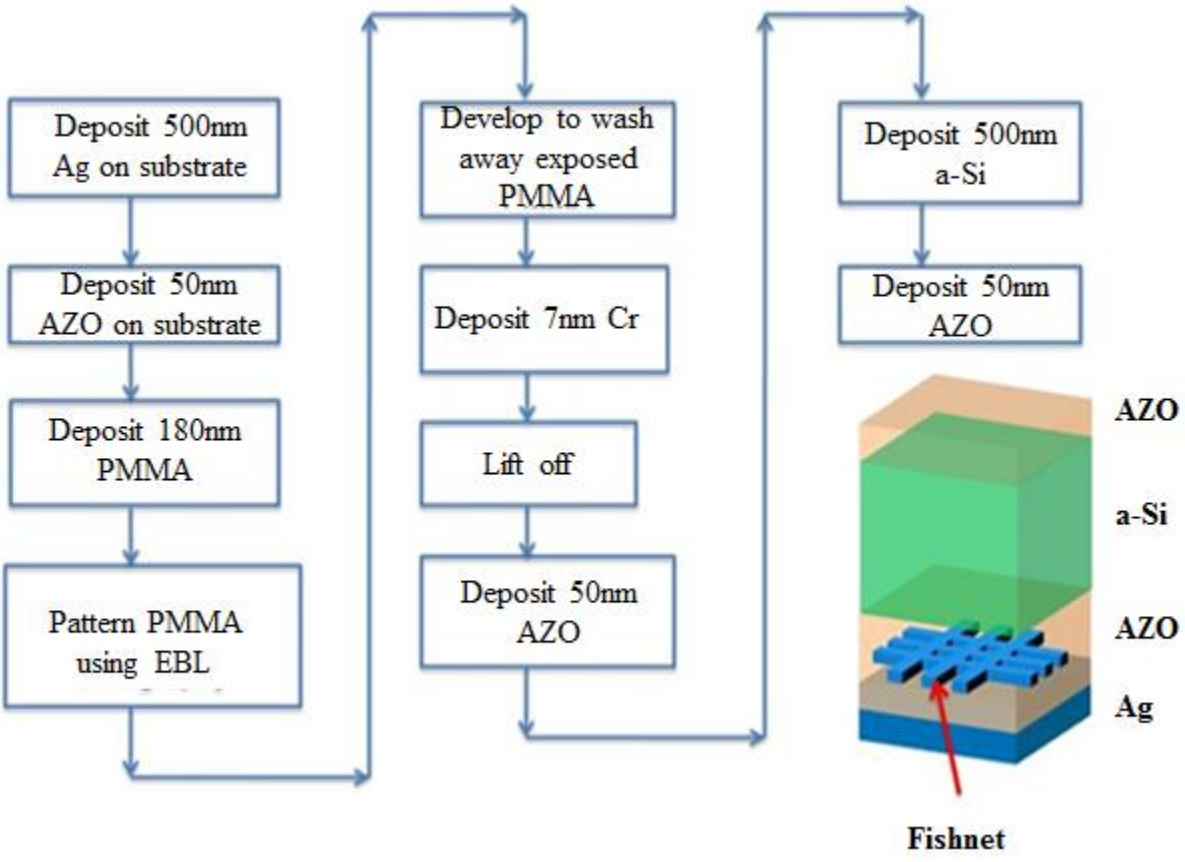

Figure 3.2: Schematic showing the fabrication process for the fishnet thin film solar cell

The most important step in the fabrication process is Electron Beam Lithography—the process that allows us to literally draw the fishnet pattern onto a substrate.

The JBX 5500ZD Electron Beam Lithography system by JEOL [Figure 3.3] was the most integral part of the fabrication of the fishnet. However we must realize that prior to pattern writing and development, there is a spin coating step. This step is extremely important to ensure that the electron beam has a stable material to write on, and also to ensure proper lift off following metal deposition. In this step, electron sensitive resist is spun onto a substrate. This is achieved by placing the substrate on the Spincoat G3P-B from Specialty Coating Systems. The special feature of this spin coater is that the spin speed can be increased according to a user defined ramp function. So the spin speed can be increased gradually resulting in a very uniform resist thickness on the surface. The variation in resist thickness was found to be within 8 nm across a 4 inch silicon wafer. The resist thickness was measured optically using the Nanospec system from Nanometrics.

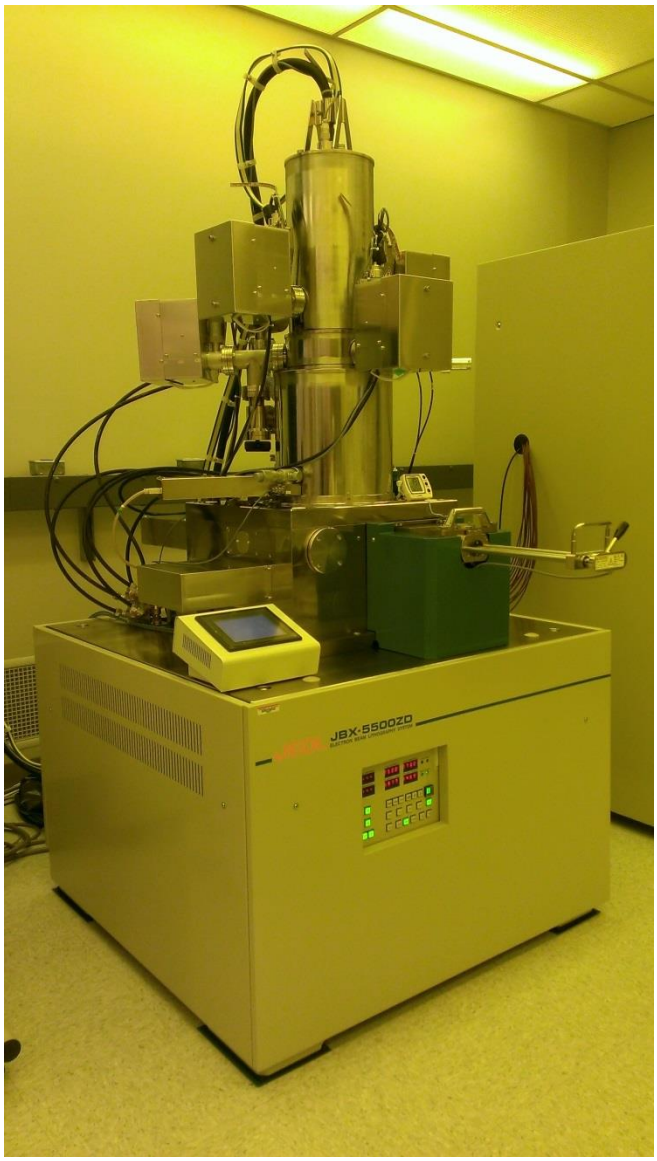

Figure 3.3: The JEOL JBX 5500ZD, High Density Electronics Center (HiDEC), University of Arkansas (Photograph by Sayan Seal, July 23, 2013)

Figure 3.4 shows a schematic of how a spin coater works. The substrate is held by vacuum on a chuck that rotates following a recipe that the user sets as input. The resist is in the form of a solution that is dispensed as a drop on the center of the substrate before the chuck starts rotating. More specifically, the resist used in this case is a solution formed by dissolving Poly-

methyl Methacrylate (PMMA) in anisole. The concentration of the solution was varied between 6% and 4%. In this recipe, the ramp, spin speed (in revolutions per minute) and dwell time (in seconds) is defined by the user. For a given set of these parameters a unique thickness of resist is coated on the substrate.

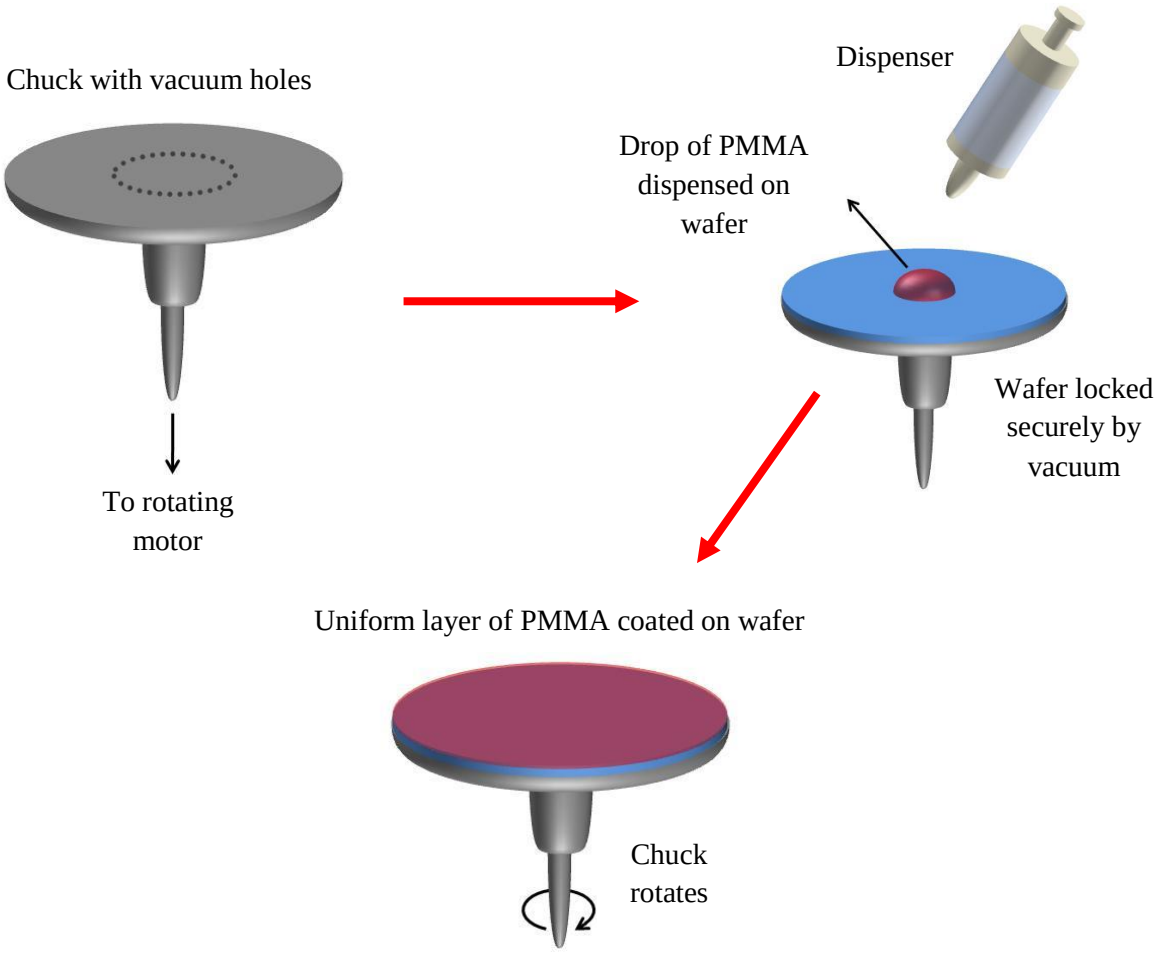

Figure 3.4: Schematic of spin coating

Ideally the resist layer should be made as thin as possible. This would allow us to use a smaller electron dose and enable us to write patterns with very small line widths, but there is an important factor to consider here. Referring to the process schematic in Figure 3.1, we find that after patterning and development, we have to deposit a 20 nm layer of silver in the empty grooves using thermal evaporation. However, there will also be a silver layer deposited atop the undeveloped PMMA. This situation is shown schematically in Figure 3.5.

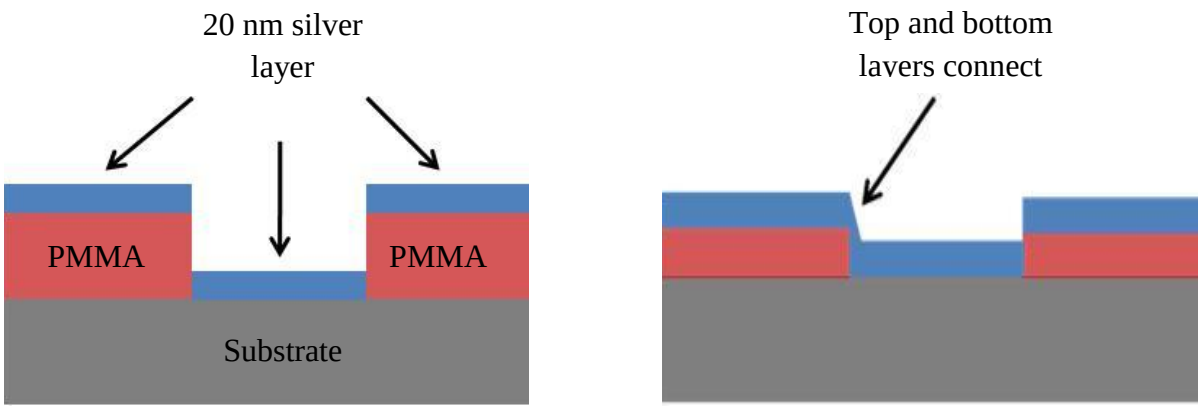

(a) Lift off will be successful (b) Lift off will fail

Figure 3.5: Schematic of metal deposition after development

After this step, the sample has to be dipped in acetone to dissolve the remaining PMMA, thus getting rid of the metal layer above the PMMA, as if we "lift off" the metal. This will leave us with a silver pattern on the substrate. For the lift off step to be successful, it needs to be ensured that the top and bottom metal layers do not touch. This will close the gap between them,

preventing the acetone from dissolving the PMMA. Hence the resist layer has to be made thick enough to prevent this from happening. Ideally the resist layer could be made very thick to prevent lift off issues, but there is a limit to doing this. For the fishnet pattern, after development we are left with a 500 nm x 500 nm square PMMA column. The height of this column is the thickness of the resist. If the resist is made too thick with respect to the base area of the column, it will collapse under its own weight. The resist thickness was chosen to be around 180 nm for this design. The recipe for spin coating is outlined in Table 3.2. The spin speed in step 5 was chosen from the spin speed curve for 4% PMMA provided by the manufacturer [Figure 3.6].

Step	**Ramp**	**Revolutions/ minute**	**Dwell Time (in s)**
Coat	0	0	2
Spread	0.5	500	2
Coverage	0.5	1000	2
Settle	0.5	500	2
Final Spin	3	4000	30
Slow down	3	200	5

Table 3.1: Recipe for spin coating

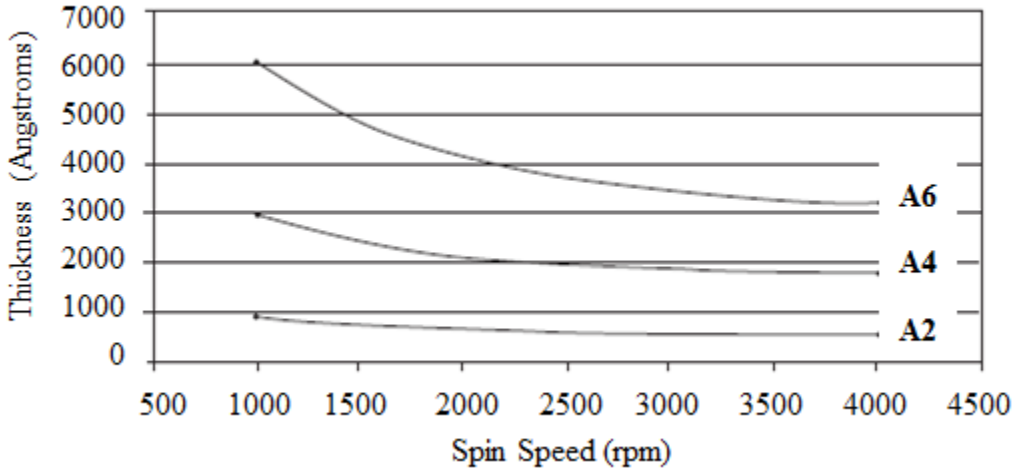

Figure 3.6: Thickness as a function of spin speed for PMMA from MicroChem

The thickness of the resist layer was measured to be around 180 nm averaged over ten measurements across randomly chosen points on the sample surface. Once the proper resist thickness is determined, the lithography process follows. In a sense, electron beam lithography (or EBL) is similar to photolithography.

The principle of EBL is in similar to photolithography in many respects. The surface of the substrate has to be spin coated with an electron sensitive resist in EBL instead of a photo sensitive one. A controlled electron beam then literally writes the pattern onto this resist. So no mask is required like in photolithography.

Before any writing is done, a design has to be made. This design can be made in AutoCAD and converted to a compatible GDSII file using LinkCAD, or the design software provided by JEOL can be used to save the design as a J01 file. For relatively simple designs like

the fishnet, the pattern designer in the JEOL software is preferable, since the design conversion step can be skipped. Following this, the GDSII or J01 file has to be converted to a v3.0 file compatible with the EBL system, which essentially divides the design into fields and subfields [Figure 3.7]. A field is like a unit cell, which when extended in the X and Y direction gives us the whole pattern. Depending on the complexity of the design, the field can be further divided into various subfields. Figure 3.8 illustrates the concept of a field using a simple schematic.

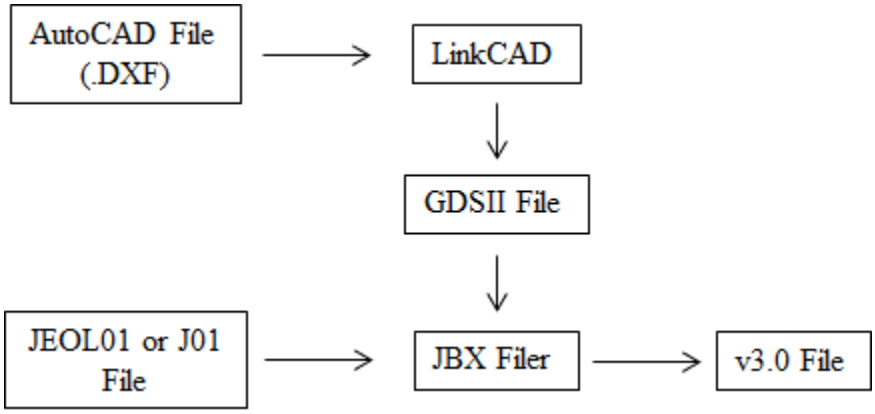

Figure 3.7: File conversion in the JEOL JBX 5500ZD

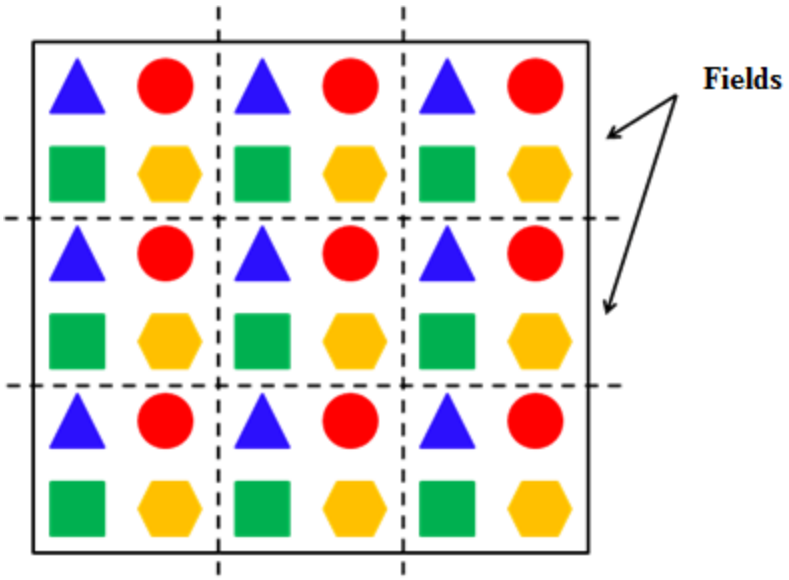

Figure 3.8: Schematic showing the concept of a field

The software searches for symmetry in the pattern and divides the entire pattern into small fields. This is done because the sample stage moves in the following way: It exposes one field to the electron beam, blanks the beam, steps to the next field, and exposes the same pattern. Through this simple step and repeat process, the entire pattern is written. For example, for the fishnet pattern the total patterned area was 1mm x 1mm with a field size of 180 μm x 180 μm. Once the design is converted to a v3.0 file, the next step is system calibration. There are two different calibration modes, either of which can be used for the JBX 5500ZD—the deflection mode and the current mode. The deflection calibration mode was used for the fishnet pattern.

It is important to obtain a brief understanding of how the EBL system works. Figure shows a simple schematic of the JBX 5500ZD system. Figure 3.9 shows a simple schematic that can be used to understand the working principle of the JBX 5500ZD.

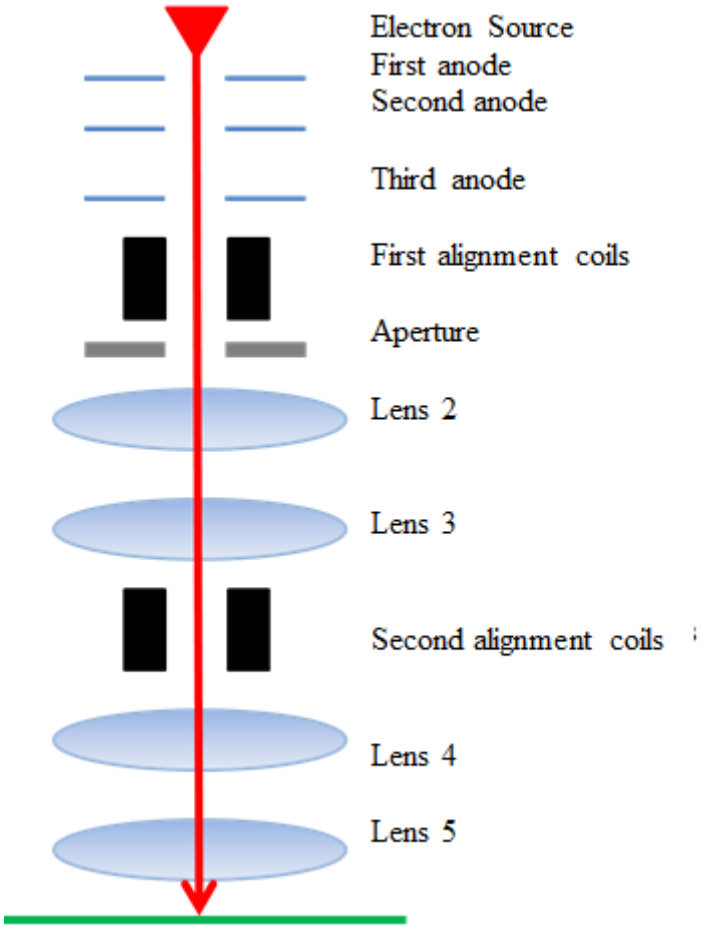

Figure 3.9: Schematic of the JEOL JBX 5500

The lens system and alignment coils constitute what is known as an Electro Optic System (EOS). The anode accelerates the electron beam from the source, which is a ZrO:Wthermal field emitter. The system uses an electrostatic deflection system to control the electron beam, and has a laser beam controlled sample stage.The input data can be entered in the JEOL52 (or v3.0) format. Based on the acceleration voltage and the objective lens used, four EOS modes can be described as shown in Table 3.2.

EOS Mode	Accelarating Voltage (in kV)	Objective Lens	Maximum Field Size (in µm)	Maximum Subfield Size (in µm)	Minimum Scan Step (in nm)	Writing Result	Writing Speed
1	25	4	2000	20	10	Rough	High
2	50	4	1000	10	5	↓	↑
3	25	5	200	2	1	↓	↑
4	50	5	100	1	0.5	High	Low

Table 3.2: Operating modes of the JEOL JBX 5500ZD

The acceleration voltage can be chosen to be either 25 kV or 50 kV. For example, using a lower acceleration voltage of 25 kV and lens 4 gives a maximum field size of 2000 µm, a relatively high minimum scan step of 10 nm, with the advantage of the fastest writing speed. In short, EOS Mode 1 is suitable for patterns of relatively larger critical dimensions, larger pitch size, and in situations where writing speed is a priority. Using a higher acceleration voltage of 50 kV confines the electron beam to a smaller area, thus giving a smaller field size. Using lens 5 serves to focus the electron beam further for patterns of really small critical dimensions. This comes at the disadvantage of a very small maximum field size, resulting in a very low writing speed. For the fishnet pattern, the critical dimension was 80 nm–100 nm, it was sufficient to use EOS Mode 2.

The major drawback of the EBL process is the time required to complete writing, even while using EOS Modes 1 or 2. It can take up to two hours to complete writing a 1 mm x 1 mm area, depending on the complexity of the design and step size of the beam. For the Fishnet

pattern the typical time required for writing was approximately 40 minutes for a 1 mm x 1mm area. However for manufacturing on a commercial scale nanoimprinting techniques are available that will be able to produce these cells at a much faster rate [64].

A 50 kV beam was used and the scan step was set to 2 nm to ensure that the pitch size was accurate throughout the patterned area. After determining the appropriate EOS mode, the next step is system calibration. In this step the electron beam is properly aligned and accurately positioned with respect to the standard alignment marks (the AE and BE alignment marks). Also the electron beam current can be adjusted during calibration. For the fishnet pattern the beam current was adjusted to 1 nA, a standard value used with EOS mode 2. Adjusting the beam current is the first step in sample alignment. Next, the position of the beam has to be accurately determined. Every time a pattern is written, the system has to be calibrated. When the EOS mode or filament current is changed, the system has to be calibrated. Every design will have a specific set of acceleration voltage, lens, and filament current. This will affect the intensity and spot size of the electron beam. The calibration process ensures that the beam spot accurately follows the design saved in the input data file.

As mentioned earlier after writing one field the electron beam writes the next field. This transition between fields takes place through a movement of the sample stage, thus making it imperative for the stage control to be precisely controlled. Figure 3.10 shows a schematic for the laser beam control for the sample stage in the JEOL 5500ZD.

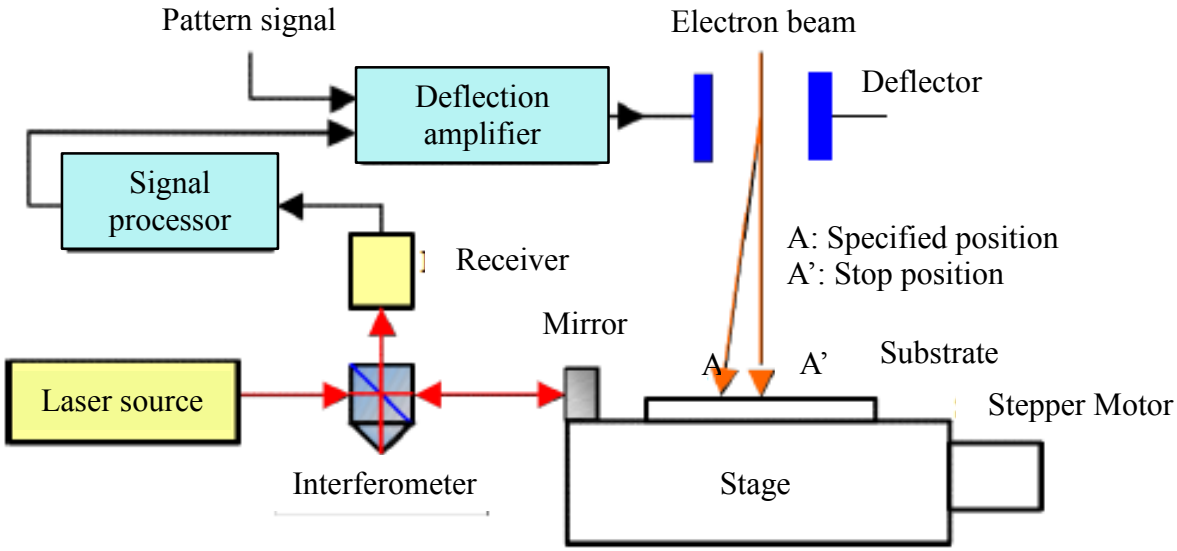

Figure 3.10: Laser beam controlled sample stage of the JEOL JBX 5500ZD as described by the equipment manual

For proper positioning of the sample stage, the system uses alignment markers known as the AE and BE alignment marks. During the calibration process, the AE and BE marks have to be located manually, focused, and their position has to be entered into the system. Based on these values, the system performs a deflection correction, which ensures that there is minimum error between the stage movement described by the software and the actual physical stage movement. Figure 3.11 illustrates the deflection correction mechanism, as described by the manufacturers user manual.

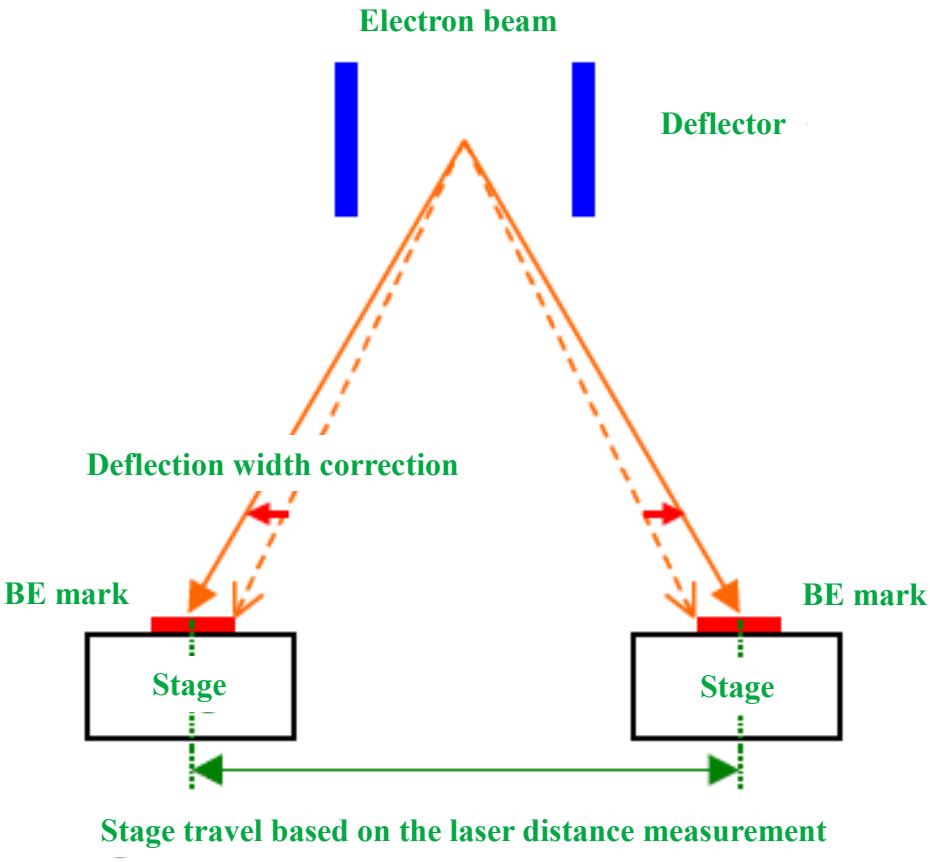

Figure 3.11: Deflection correction in the JEOL JBX 5500ZD as described by the equipment manual

The final step was exposure. The v3.0 file containing the design was loaded onto the exposure window. This pattern has dimensions equal to the chip size of 180μm specified in the design file, so it had to be laid out in a 6x6 two dimensional array to form a 1.08 mm x 1.08 mm pattern. After the final array was made the exposure dose, scan step and calibration mode had to be determined.

The scan step is the step size of the beam and was fixed at 2 nm. The calibration mode, as mentioned earlier, was set to deflection mode. The number of electrons incident on the resist per square cm is defined as the dose. It is measured in $\mu C/cm^2$. The dose has to be optimized for a particular design. If the dose is too low, the intensity of the electron beam will not be enough to expose the resist thoroughly. This condition is called "underexposure". Also if the dose used is too large, it results in the electron beam spreading laterally within the resist layer, thus widening the feature size. This condition where the electron beam burns into the resist layer is called "overexposure". Determining the correct electron dose is only half the story. Similar problems of residual resist or over etched resist can also be caused by an improper development process, which will be discussed in due course.

For the fishnet structure was varied from 500 $\mu C/cm^2$ to 1500 $\mu C/cm^2$. The best results were obtained for a dose of 800 $\mu C/cm^2$. Basically obtaining a successful pattern is a combination of the resist thickness, electron dose and development time. Once the exposure dose is entered into the software the pattern is ready to be exposed on the substrate. After a writing time that typically spanned 45 minutes for a 1mm x 1mm fishnet pattern, the sample was unloaded and developed.

Development is defined as the process by which exposed resist is washed away by a chemical known as a developer. This developer reacts selectively with regions that are exposed to the electron beam and unexposed areas. The sample is usually dipped in a bath containing the developer solution for a fixed time called the development time. The development time changes depending on the design. If sufficient time is not allowed for development, the exposed resist is left behind in clumps and the process is said to be "underdeveloped". Similarly, when the sample

is kept dipped in the developer in excess of the development time, the developer starts to etch the unexposed areas as well, thus widening the exposed features. In this case the process is said to be "overdeveloped".

The final development time for a 1 mm x 1 mm fishnet pattern was 25 seconds, given the resist thickness and exposure dose. After development there was a fishnet shaped groove in the PMMA layer. The sample was washed using IPA for 30 seconds to remove any residual developer within the grooves and the sample was blown dry using nitrogen. Following this the resist was baked at 100ºC on a hot plate for 60 seconds. This evaporates any moisture or organic residues present in the sample, as well as it makes the PMMA columns more rigid structurally. Care must be taken not to hard bake the resist on to the substrate, so as to prevent proper lift-off. A period of 60-90 seconds is deemed appropriate according to the manufacturers data sheet [Reference].

The next step was to evaporate metal onto the grooves to obtain a metallic fishnet structure on the substrate. The sample was loaded onto a thermal evaporator. According to design specifications, the thickness of the fishnet should be 20 nm, but it was found that thin films of silver had issues adhering to the AZO surface. So a 7 nm layer of chromium was used below the silver layer to promote adhesion. Once evaporation was completed a lift off had to be performed

3.3 Measurement of Total Absorption of the Thin Film Solar Cell With and Without the Fishnet Structure

After fabricating the sample, the next step is to measure the amount of light absorbed by the sample. The sample has a metal back electrode; hence the transmission through the sample will be practically zero. Under these circumstances, if the fishnet does indeed work as a plasmonic scatterer, we should observe an increase in total absorption at the resonance frequency. The reflection from the sample was measured using a Spectroscopic Ellipsometer. Since transmission is negligible, we can safely assume that the rest of the light is absorbed by the sample. There may be a concern here that the total absorption does not accurately represent the power actually absorbed in the a-Si layer. It also includes the losses that take place in the fishnet structure, AZO layers and the back electrode. In Chapter 4, results will be presented which prove that as much as 83% of the total light absorption occurs within the a-Si layer. Thus it is correct to measure the reflection off the top of the sample, and calculating transmission from it. For reflection measurement a Variable Angle Spectroscopic Ellipsometer was used. Ellipsometry is a widely used material characterization, and the measurement is essentially reflection based. Thus it can also be used to measure reflection and transmission. Both the material characterization and reflection measurement features have been used in this project.

The equipment is manufactured by the J. A. Woollam Company in Lincoln, Nebraska, USA. Figure 3.10 shows a photograph of the V-VASE system installed at the Microwave and Optics Laboratory for Imaging and Characterization, University of Arkansas.

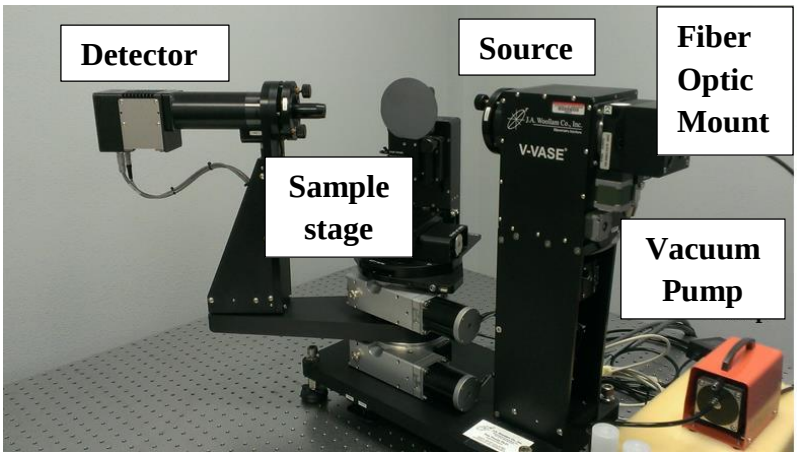

(a) V-VASE system at the University of Arkansas, Fayetteville.

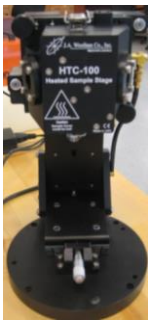

(b) Heat stage

(c) Rotating stage

(d) Focus probes mounted on the source and detector units

Figure 3.12: Components of the V-VASE system from the J. A. Woollam Co. (Photograph by Sayan Seal, July 12, 2013)

Apart from the sample stage shown in Figure 3.12 (a), the ellipsometer can also be operated with a host of other stages like the heat stage for temperature dependent measurements [Figure 3.12 (b)], and the rotating stage for anisotropic samples [Figure 3.12 (c)]. The source ranges from 190 nm to 2500 nm, and can be varied in steps of 1 nm. The beam spot size is 0.5 cm when the alignment detector is present and 250 µm with the focusing probes mounted. Figure (d) shows the focus probes mounted on the source and detector units. Since the fishnet was fabricated on a 1mm x 1mm area, it was necessary to use the focus probes to shrink focus the beam to a 250 µm spot within the fishnet area. Figure 3.13 shows the beam spot confined within the area in which the fishnet pattern was fabricated. The picture shows the top view of a complete fishnet solar cell structure. This patterned area appears as a dark square in the figure, whereas the white square coincides with the area of the beam spot. The image was taken using a camera mounted on the sample stage and operated using the JAW-Cam software.

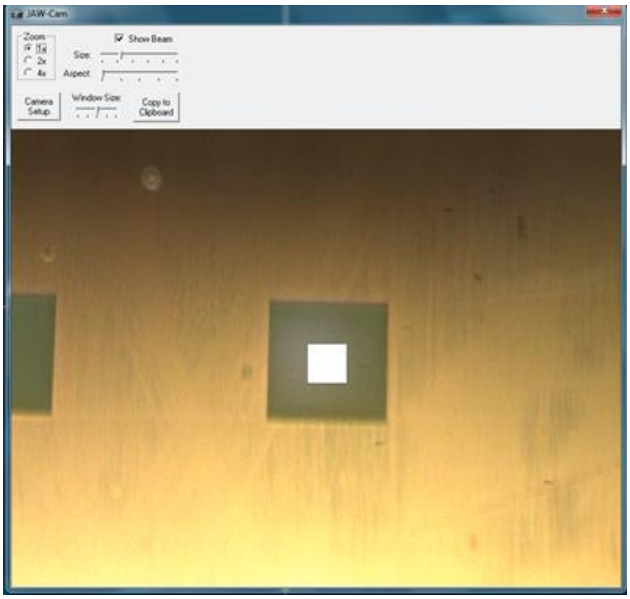

Figure 3.13: Beam spot positioned within the fishnet pattern area (Photograph by Sayan Seal, July 12, 2013)

As with most optical measurement systems, the first step is sample alignment. This ensures that the light entering the detector from the source is at a maximum. In ellipsometry, the first sample that is mounted and aligned is always the standard sample, which is a 4 inch silicon wafer with a 250Å oxide layer on the surface. This sample is used to calibrate the system. Calibration is a two-step process. The first par is the alignment in the plane of the sample or the X-Y alignment. This is accomplished by rotating the X and Y tilt screws of the sample stage, until the red cross mark on the screen is positioned accurately at the center [Figure 3.14(a)]. Once this has been achieved the sample has to be aligned in the plane perpendicular to the sample. This is known as the Z-alignment. To align the sample properly, the micrometer screw on the sample stage has to be rotated slowly to translate the sample stage along the Z-direction. This process is continued until the detector records the maximum signal, as shown in Figure 3.14 (b). Both the X-Y and Z-alignment procedures are performed to make sure that the beam is aimed properly at the detector iris after reflecting off the sample surface.

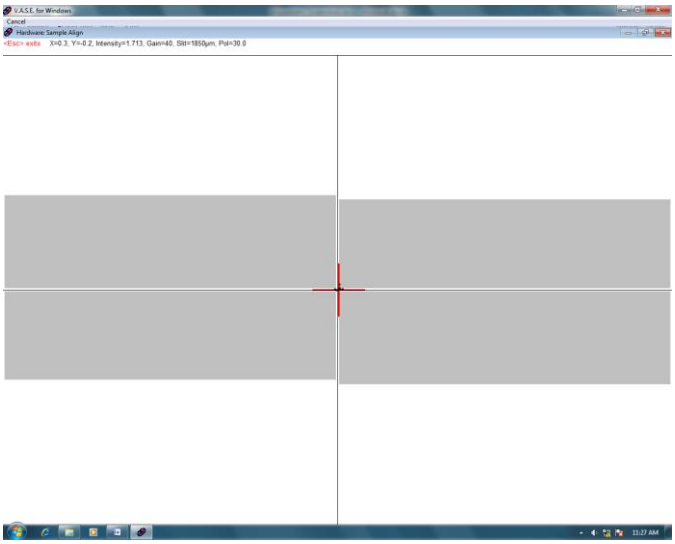

(a): Screenshot of the X-Y alignment process in the WVASE software

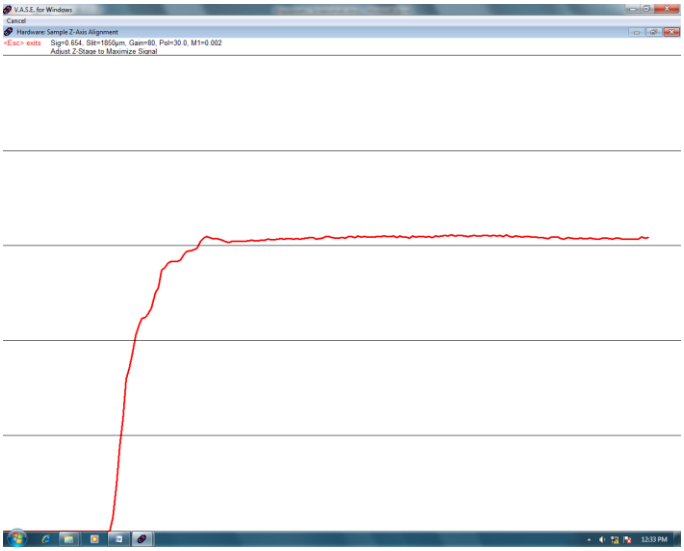

(b) Screenshot of the Z-alignment process in the WVASE software

Figure 3.14: Alignment process for the V-VASE system

In ellipsometry the incident light is polarized in a direction either perpendicular to (s-polarization) or parallel to (s-polarization) the plane of incidence. This makes it necessary for the polarizers to be calibrated accurately before taking measurements. This step is known as system calibration. In this step the standard sample is mounted and aligned, after which the system is calibrated based on reflection obtained from the sample. The nature of reflected light is a known quantity and the measurements obtained are fitted to these known results. If the resulting error is less than the prescribed limit, sample calibration is successful. There will be issues with sample alignment if the source intensity is too low. This is indicative of the fact that the alignment of the source or sample (or both) is not satisfactory. Hence it is very important to get the alignment step right before proceeding to calibration. Figure 3.15 shows the calibration data fits for the Fourier coefficients α, β, and the residual function of the intensity of light on the detector.

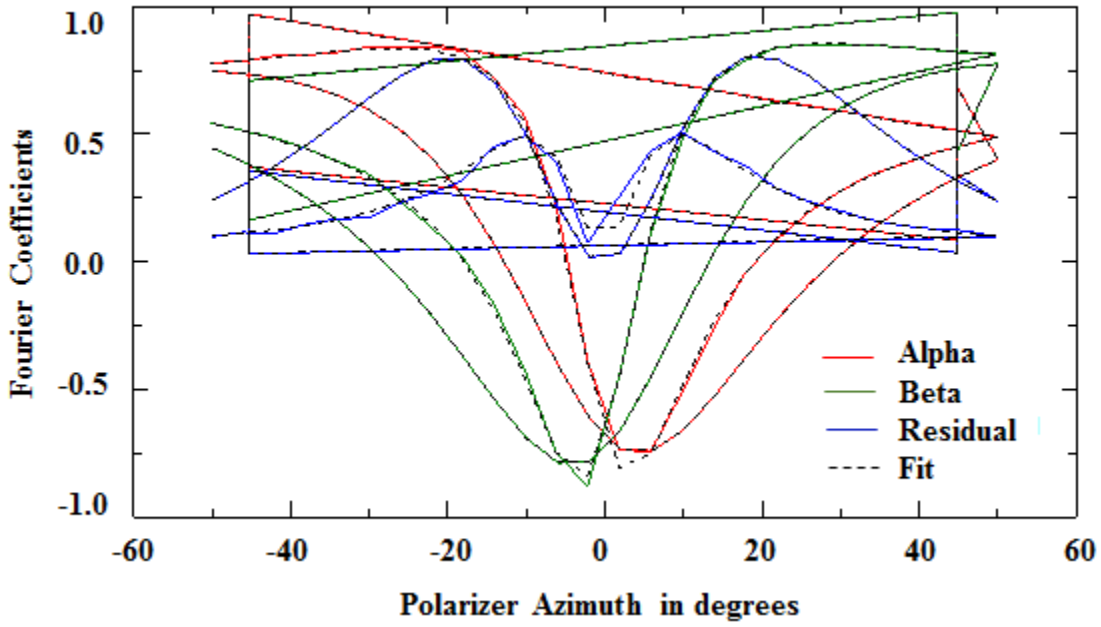

Figure 3.15: Graph showing accurate fits between measured and fitted calibration data

It is important to note here that while using the focus probes, the probes have to be aligned and calibrated separately. The focus probes should be installed only after the sample has been aligned. Following this, the X-Y alignment screws on the source and detector mounts have to e adjusted for maximum signal

After calibration, the system is ready for measurements. Material characterization andreflection measurement will be discussed in detail in sections 3.3 A and 3.3 B respectively.

3.3(A): Material Characterization

As stated earlier, the incident light from the source is polarized. When this light hits the sample surface, its state of polarization changes depending on the nature of the sample. The ellipsometer measures this change in terms of two variables, Ψ and Δ. These ellipsometer measures a quantity ρ, which can be expressed in terms of Ψ and Δ by the following relation,

$$\rho = \frac{R_p}{R_s} = \tan(\Psi) e^{i\Delta}$$

Where, R_p and R_s are the reflection coefficients of p- and s- polarized light respectively. The brief description of these polarization states will be given in due course. The values of Ψ and Δ are measured as a function of wavelength and a mathematical model is constructed to fit a curve to these data sets. This model has the optical constants and thickness of the layers of the sample as input. Once a best fit model for a given data set is obtained, the optical constants can be calculated.

3.3(B): Reflection Measurements Using an Ellipsometer

Reflection measurement using an ellipsometer consists of two parts. The first step is called a "baseline" measurement, which essentially gives us a measure of the ambient light present in excess of the signal from the source. The sample used for the baseline measurement should be very well characterized for optical properties. The calibration sample was used as the baseline sample for this experiment, and the results are presented in Figure 3.16. However, it is not necessary to use the calibration sample for the baseline measurement. The only condition is that the sample used for baseline measurement should be well characterized in terms of optical properties. Figure 3.17 shows the fit of psi and delta for the standard sample. The mean square error of the fit is 0.3919.

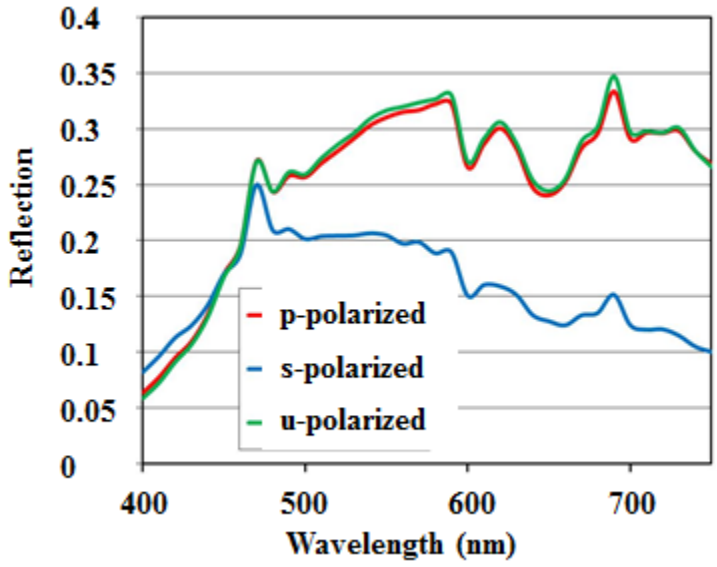

Figure 3.16: Baseline measurement for ambient light

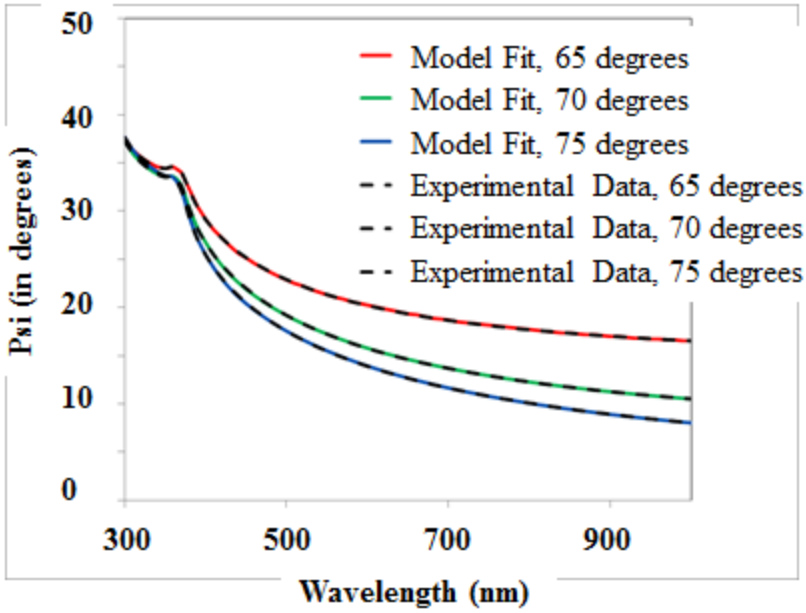

(a) Fit for Ψ for the standard sample

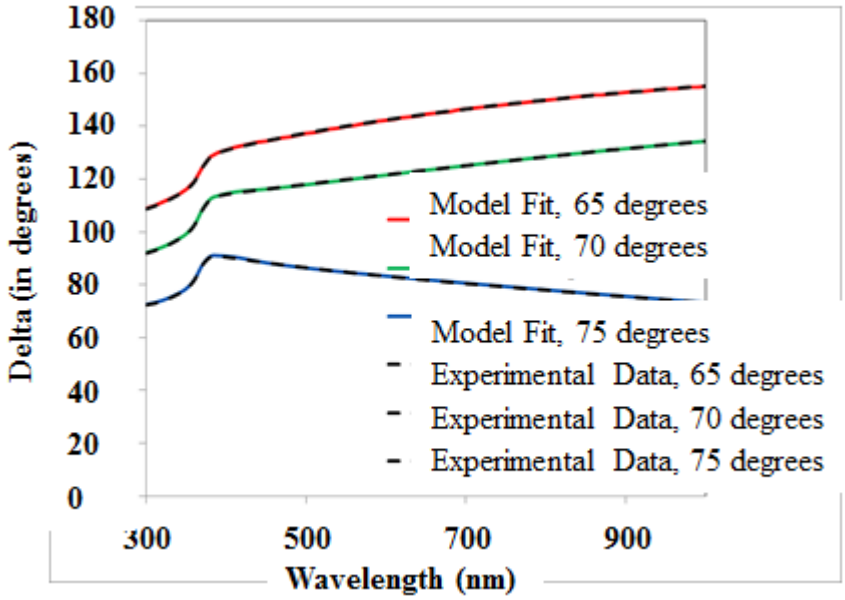

(b) Fit for Δ for the standard sample

Figure 3.17: Fit for Ψ and Δ for the standard sample

The angle of incidence for the baseline measurement has to be the identical to the angle of incidence to be used for the actual sample. In addition, measurements should be taken at the same wavelength points for the calibration sample and the actual sample. This is understandable since the intensity of source is unique for a specified wavelength point, and this practice facilitates correction for ambient light. The angle of incidence for reflection measurements was kept fixed at 15°. Ideally the reflection at normal incidence should be measured, but 15° is the smallest angle of incidence achieved by the V-VASE system.

After the baseline measurement the Fishnet TFSC was mounted and aligned on the sample stage. The reflection was measured and corrected using the baseline correction software in the WVASE software. This changes the absolute reflection measured in random units into reflectance, giving us the fraction of incident power that is reflected off the sample surface. The transmission through the fishnet sample is negligible and is shown in Figure 3.18. Thus for all practical purposes, the absorption can be expressed as (1 – Reflection).

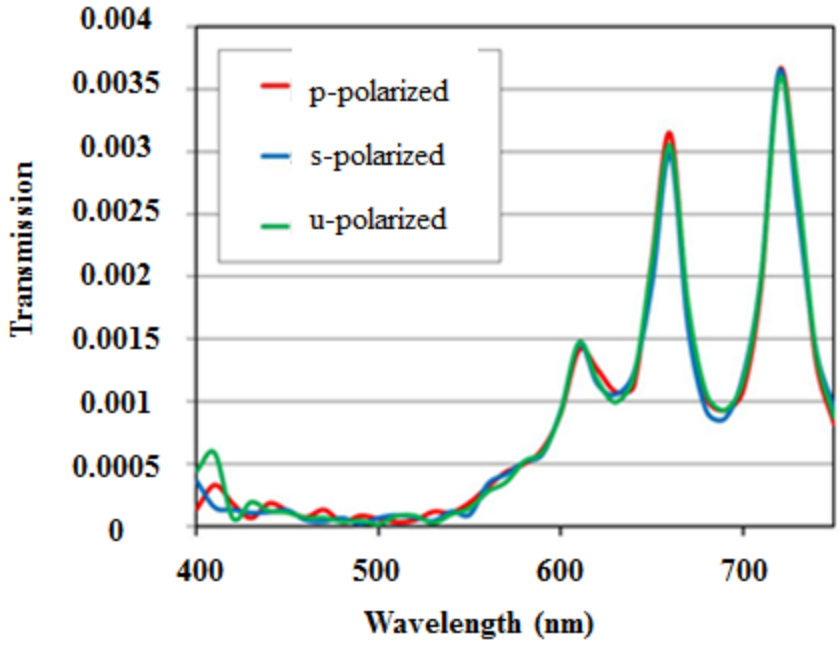

Figure 3.18: Transmission through the fishnet TFSC

Four identical fishnet TFSC's were fabricated to test the repeatability of the results obtained above. This provides confirmation of two facts (i) the fabrication recipe is repeatable, and (ii) The reflection measurement is accurate.

The measurement of reflection was done for three different states of polarization:

(i) **p-polarization:** When the electric field vector of light is parallel to the plane of incidence, it is termed p-polarization.

(ii) **s-polarization:** When the electric field vector of light is perpendicular to the plane of incidence, it is termed s-polarization.

(iii) **u-polarization:** When the electric field vector of light makes some specific anglewith the plane of incidence, it is termed u-polarization. This is a user-defined angle that can be changed in the WVASE software before taking measurements. It can range from 0° (p-polarized) and 90° (s-polarized).

3.4 Modification of the Numerical Model and Comparison with Experimental Results

As a first step the different materials used to fabricate the Fishnet TFSC, namely, silver, Al-doped zinc oxide, amorphous silicon and chromium were characterized for optical constants using ellipsometry. Note that chromium was used as an adhesion layer below the silver fishnet, but the original theoretical model did not take this into account. A 7 nm thick chromium fishnet was created below the silver fishnet in the new model. For the characterization of these materials, the following samples were used:

1) A 200 nm film of silver thermally evaporated on a silicon substrate
2) A 20 nm AZO film on a silicon substrate deposited by DC sputtering.
3) A 500 nm thick film of amorphous silicon deposited on a silicon substrate by Plasma Enhanced Chemical Vapor deposition (PECVD) technique.
4) A 100 nm film of Cr deposited on a silicon substrate by thermal evaporation.

While fabricating the test samples, an effort was made to ensure that the following parameters were kept identical with respect to the fabrication of the Fishnet TFSC,

1) Equipment used

2) Materials used

3) Thickness of deposited layers

After characterizing these materials, the optical constants obtained were used in HFSS simulation to investigate whether it caused a better agreement between theory and experiment. For the TFSC with fishnet, it was verified using Atomic Force Microscopy (AFM) that the AZO layer covering the fishnet would not be flat, but would have a fishnet size bump over the area where the fishnet was present. This factor was also considered in the numerical model in conjunction with the ellipsometry-determined optical constants. The result of this numerical simulation was compared to the experimental results.

Chapter 4: Results and Discussions

The results of the experimental procedures described in Chapter 3 will be presented in this chapter, and will be presented in the same order in which the experiments were described. In the first section, the results of numerical simulation will be presented. These will include plots for total absorption, layer-wise absorption in the cell, and plots showing the electric field within the a-Si layer. The results of the fabrication of the fishnet will be presented next, followed by the third section in which the results of absorption measurement will be shown. The final section consists of a comparison between the theoretical and experimental results, as well as a discussion on making the results match better.

4.1. Design of the Thin Film Solar cell with a Fishnet Structure in the Back Spacer Layer

The design and simulation of the TFSC was done using the High Frequency Structure Simulator (HFSS), a 3-D finite element simulation tool by Ansys, Inc. In this study, silver was the chosen as the material for the fishnet and numerical optimizations were performed to obtain a linewidth of 100 nm. Figure 3.1(a) shows the total absorption of the Fishnet TFSC plotted as a function of wavelength, contrasted with the absorption from a planar TFSC without the fishnet.

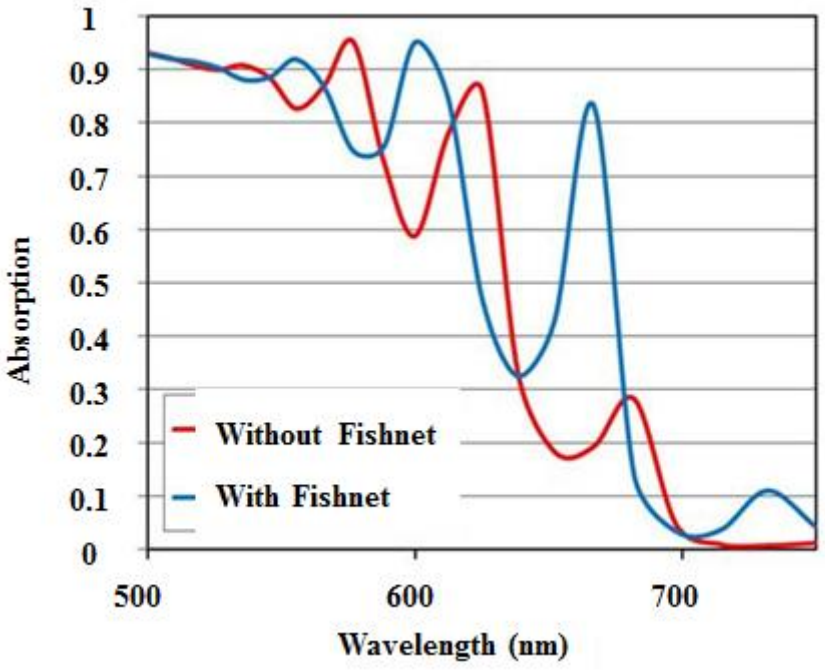

(b) Total absorption of the TFSC with and without the Fishnet

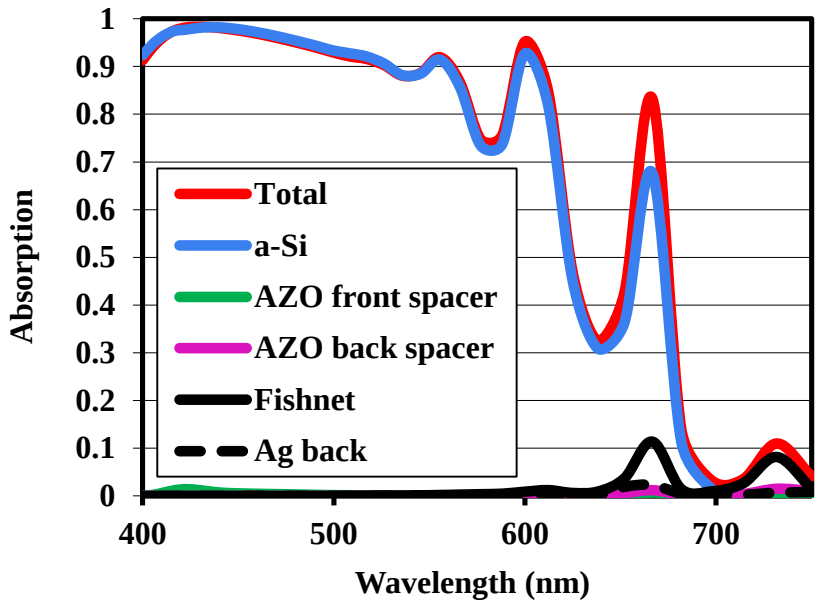

(b) Layer-wise absorption in the TFSC with the Fishnet

Figure 4.1: Numerical simulation results of the fishnet solar cell in HFSS

It is important to note that increased total absorption does not amount to an increase in absorption by the a-Si layer. It is the absorption in the a-Si layer that contributes to carrier transport and enhances the electrical characteristics of the thin film solar cell. Hence it is important to verify that the loss in the fishnet is low. So a complete layer-by-layer analysis of absorption was done in HFSS, which verified that nearly 82% of the total absorption was in the a-Si layer, with only 18% dissipated as loss in the fishnet, AZO and the silver back electrode combined. The results of this analysis are presented in Figure 4.1(b).

Further proof of the fact that the fishnet structure results in an enhancement in absorption in the a-Si layer is obtained by studying the electric field pattern within the absorber layer at the resonance frequency. Figure 4.2 shows a comparison of the normalized electric field in the a-Si layer with and without the fishnet. The simulation was done using HFSS. It was observed that using the fishnet structure concentrates the electric field within the a-Si layer.

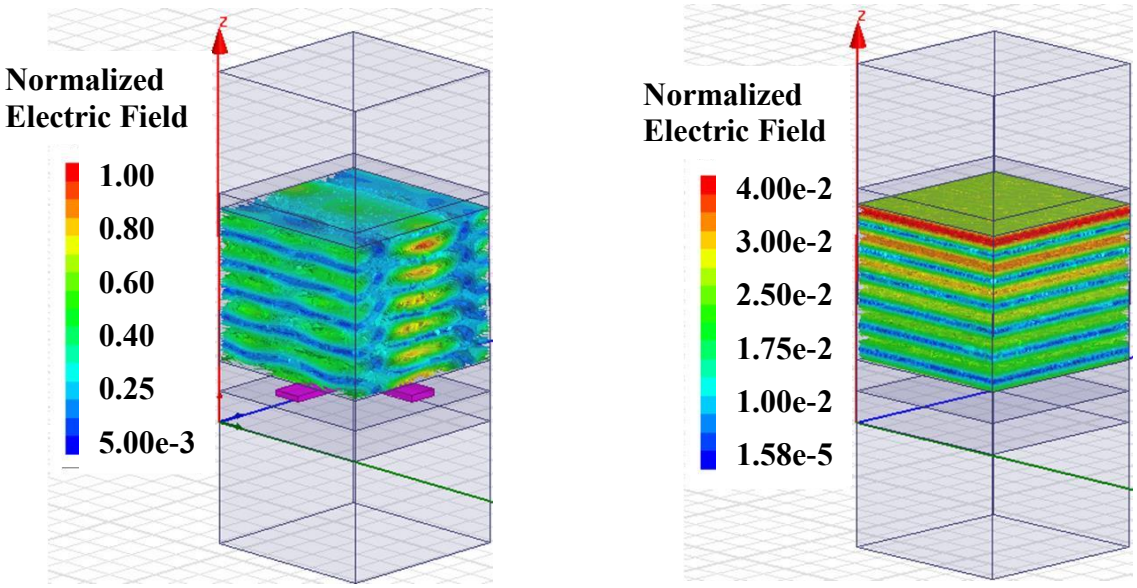

(a) with fishnet (b) without fishnet

Figure 4.2: Electric field in the a-Si layer of the fishnet TFSC computed using HFSS

At this point the design looked convincing enough to consider fabricating a complete thin film solar cell structure. The principal challenge of making this structure was the fabrication of the fishnet structure. The following sections will discuss the fabrication of the Fishnet TFSC in greater detail.

4.2 Fabrication of the Fishnet Pattern using Electron Beam Lithography

The optimized design for the silver Fishnet structure had a linewidth of 100 nm. It was not possible to use photolithography since the system at the **Hi**gh **D**ensity **E**lectronics **C**enter (HiDEC) at the University of Arkansas could do no less than 2.5 microns in terms of linewidth given the design at hand. Hence Electron Beam Lithography (EBL) was used. The details of the fabrication process have been explained in detail in Chapter 3. Pictures of the fishnet structure were taken using Scanning Electron Microscopy (SEM). The images were taken after the lift off step following metal deposition. The pictures show the top view of the silver fishnet on the surface of the substrate.

Figure 4.3 shows the result obtained in the first trial. A dose of 1500 $\mu C/cm^2$ was used initially and the fishnet was patterned on a 550 nm thick layer of resist. A clean and uniform, with no residues or defects pattern can be seen in the image. But the linewidth turned out to be much larger than expected. An average linewidth of 200 nm was obtained, which was double that in the design.

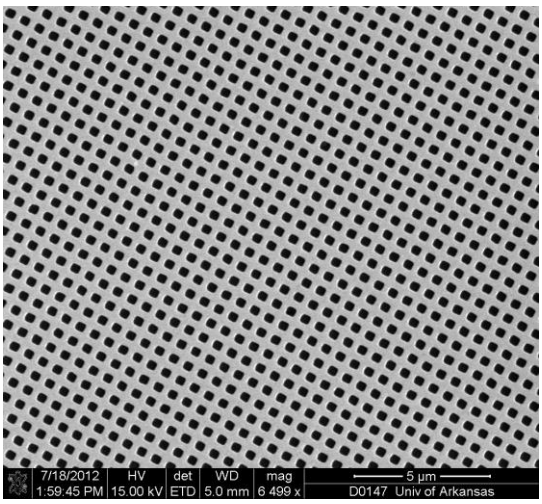

Figure 4.3: SEM pictures for a dose of 1500 μC/cm^2 and a design linewidth of 100 nm

There were two factors that caused this:

(1) The dose was too high. This resulted in the lateral spreading of the electron beam in the resist layer and resulted in an increase in the linewidth.

(2) The development time was longer than necessary. This causes the developer to etch in to the sidewalls causing the linewidth to become wider.

An easy fix for this condition would be to reduce the design linewidth in the software, but that would not give us an estimate of how close we could get to the targeted linewidth without manipulating the design. So as a next step the dose was reduced to 1000 μC/cm^2. Figure 4.4 shows the SEM picture of the pattern. It turns out that using a smaller dose ends up underexposing the resist. The developer cannot wash away most of the exposed regions and hence we get patches of silver when we evaporate metal onto the sample.

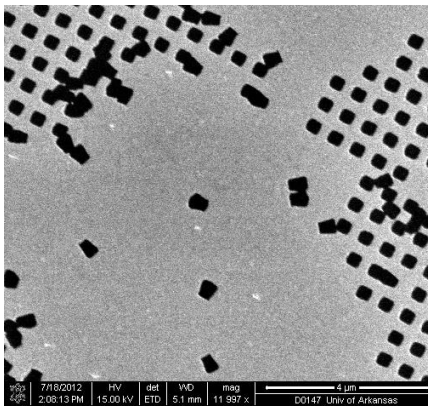

Figure 4.4: Using a smaller dose results in underdeveloped pattern

It was clear that we needed a smaller dose to achieve a smaller linewidth. One wayto do this and ensure that the resist was adequately exposed was to make resist layer thinner. Hence a 4% solution of PMMA in anisole was used with a faster spin speed to get a thinner layer of resist. The curve shown in Figure was used to determine the spin speed. It is observed that a speed of about 4000 rpm would give a thickness of just under 200 nm. The same recipe described in Table 3.1 was used, but the spin speed during final spin was changed to 4000 rpm. The thickness averaged over ten measurements was found to be 180 nm.

Once again a dose of 1000 $\mu C/cm^2$ was used, but this time the development time was varied. Since the resist layer was thinner, lesser time would be required to wash off lesser material during development. Three samples were fabricated and the development time was reduced for each sample. The results are shown in Figure 4.5.

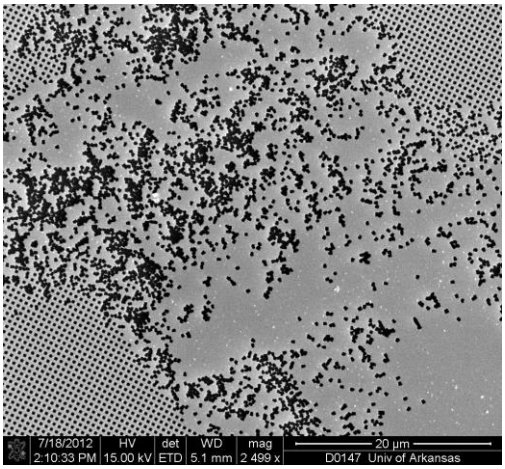

(a) Development time = 40 seconds

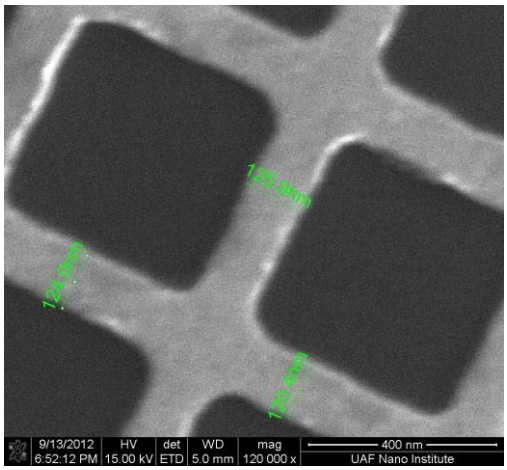

(b) Development time = 35 seconds

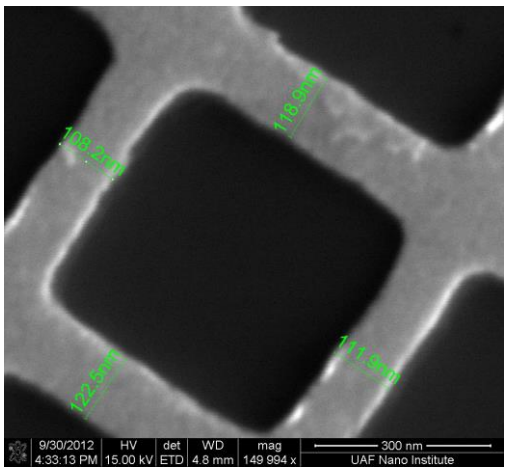

(c) Development time = 30 seconds

Figure 4.5: Optimization of development time

A development time of 35 seconds worked best giving a linewidth of 115 nm. However the linewidth was not uniform over the entire pattern and varied between 108 nm to 123 nm. 30 seconds gave narrower linewidths but regions around the corners showed signs of underdevelopment [Figure 4.5(c)].

At this point the design linewidth of 100 nm in the software was reduced to counteract the excess width on the fabricated sample. We were sufficiently close to 100 nm to be able to take this step. After that it would just be a question of calibrating the dose and the recipe would be ready. The design linewidth was reduced to 85 nm. The same dose of 1000 $\mu C/cm^2$ but a development time of 30 seconds was used. Note that the development time was also slightly reduced. Due to the reduction in the design linewidth, the beam will expose lesser volume of resist; hence we would require less time to wash off the exposed resist. The result of this process is shown in Figure 4.6.

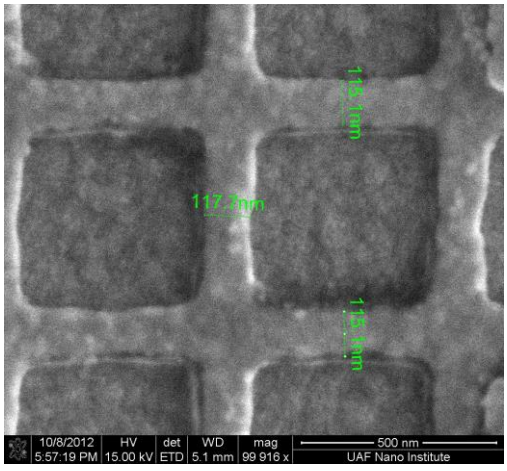

Figure 4.6: Design linewidth reduced to 85nm, development time reduced to 30 seconds

The linewidth obtained was still around 115 nm, but there was much more consistency in the linewidth than before.

Lastly, a dose optimization was performed to get down to 100 nm. Keeping the design linewidth and development time constant at 85 nm and 30 seconds respectively, the dose was changed from 500 μC/ cm^2 to 800 μC/ cm^2 in steps of 100 μC/ cm^2. From the results [Figure 4.7], it can be observed that a dose of 800 μC/ cm^2 gave an average linewidth of about 105 nm. Using a dose smaller than this resulted in underexposure.

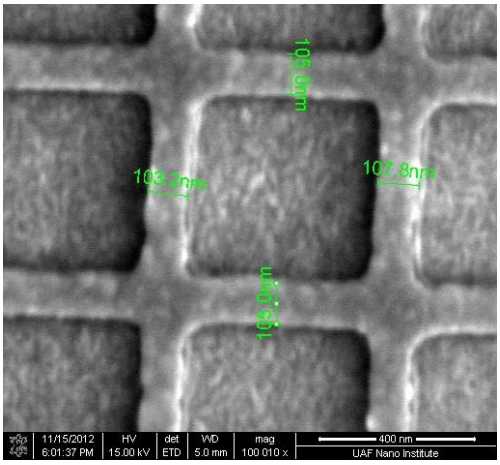

(a) Dose = 800 μC/ cm^2

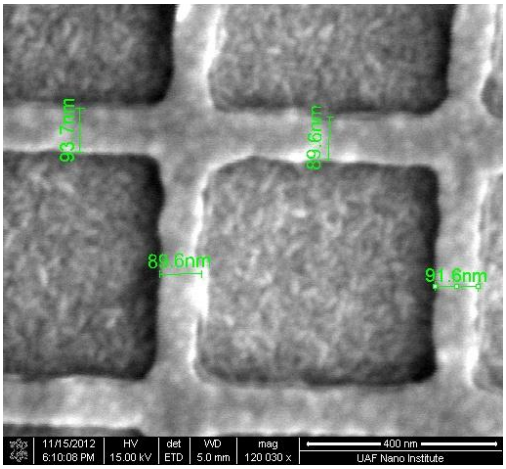

(b) Dose = 700 μC/ cm^2

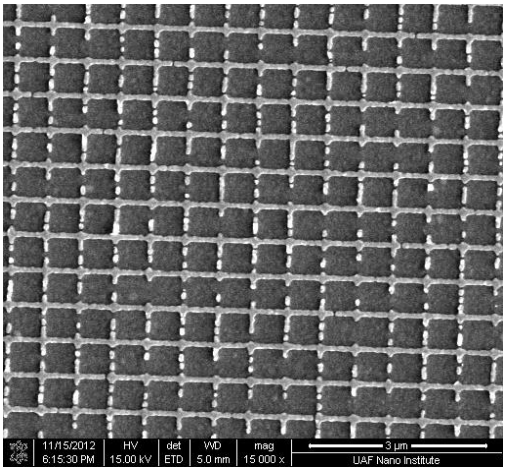

(c) Dose = 600 μC/ cm^2

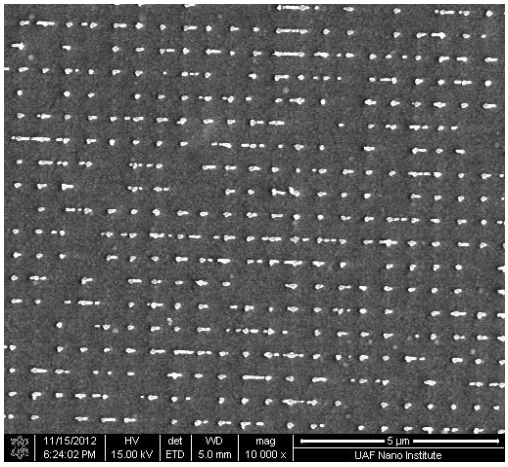

(d) Dose = 500 μC/ cm^2

Figure 4.7: Final dose optimization step

At 700 nm the linewidth dropped below 100 nm, and for lower doses there were problems of underexposure. At a dose of 800 nm, the recipe worked perfectly yielding a linewidth of 105 nm on an average. It was expected that using a marginally shorter development time could give us a perfect 100 nm linewidth. The best results were obtained using a

development time of 25 seconds [Figure 4.8]. The linewidth was found to be uniformly 100 nm at the center of the pattern as well as the corners, with proper lift off across the entire patterned area. Also a consistent pitch size of 598 nm was obtained.

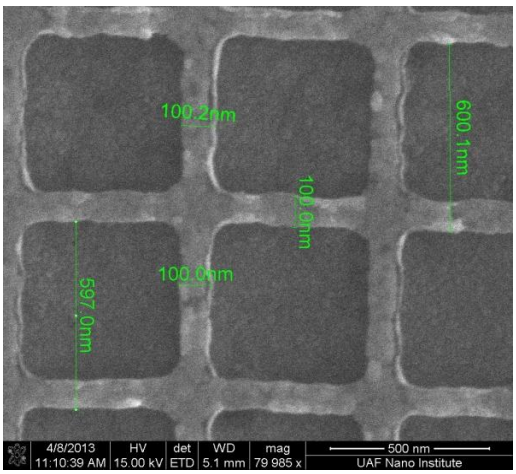

(a) Linewidth = 100 nm

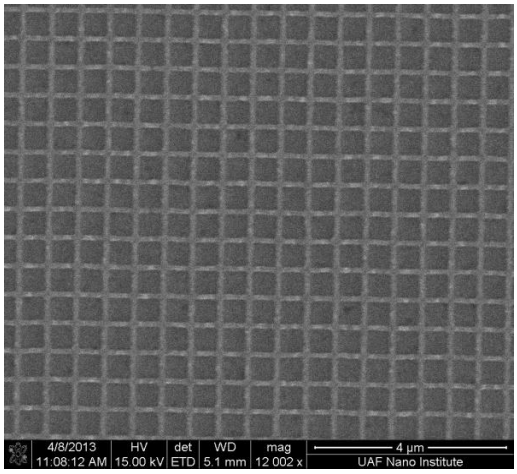

(b) Pattern uniform over whole area

Figure 4.8: 100 nm linewidth pattern using a dose of 800 μC/ cm^2, design linewidth of 85 nm, and develop time of 25 seconds.

The above recipe was repeated on at least eight fishnets to make sure that a repeatable and reliable fabrication process was developed. The SEM showed the same 100 nm linewidth for all samples that were fabricated using the above recipe. Following the fabrication of the fishnet, the rest of the steps in Figure 3.1 had to be completed to obtain a complete thin film solar cell structure. 50 nm of AZO was deposited using DC sputtering, followed by 500 nm a-Si using PECVD. The 50 nm AZO front spacer was deposited using DC sputtering as well. Thus the fabricated structure optically resembled a thin film solar cell in all respects.

4.3 Measurement of Total Absorption of the Fabricated Samples

After a repeatable fabrication process for fabricating the fishnet solar cell was established, the next step was to measure the absorption in this sample and determine whether there is an enhancement. As a control sample a planar TFSC was used, i.e., a thin film solar cell minus the fishnet. All other layers were the same and were of the same thickness as previously described.

The details of the measurement method have been discussed in detail in Chapter 3. It is worth mentioning here again that measuring reflection from the top surface is not a faithful representation of total absorption. Figure 3.1 shows the layer-wise absorption in a Fishnet TFSC. It was clearly established through numerical simulation in HFSS that 82% of the total absorption occurs within the a-Si layer.

A 4 inch silicon wafer with a 250Å oxide layer on the surface was used to calibrate the system. Following the calibration step the "baseline" measurement is performed to get a measure of the ambient light present. The angle of incidence for the baseline measurement was kept fixed at 15°. Measurement at normal incident would be ideal but 15° is the smallest angle of incidence that can be achieved by the V-VASE system.

After the baseline measurement the Fishnet TFSC was mounted and aligned on the sample stage. The reflection was measured and corrected using the baseline correction software in the WVASE software. The absorption spectrum if the Fishnet TFSC contrasted with a comparable planar TFSC is shown plotted in Figure 4.9.We observe a 12.8x enhancement in total absorption near

the band gap of a-Si. There is also significant enhancement observed across the entire wavelength range.

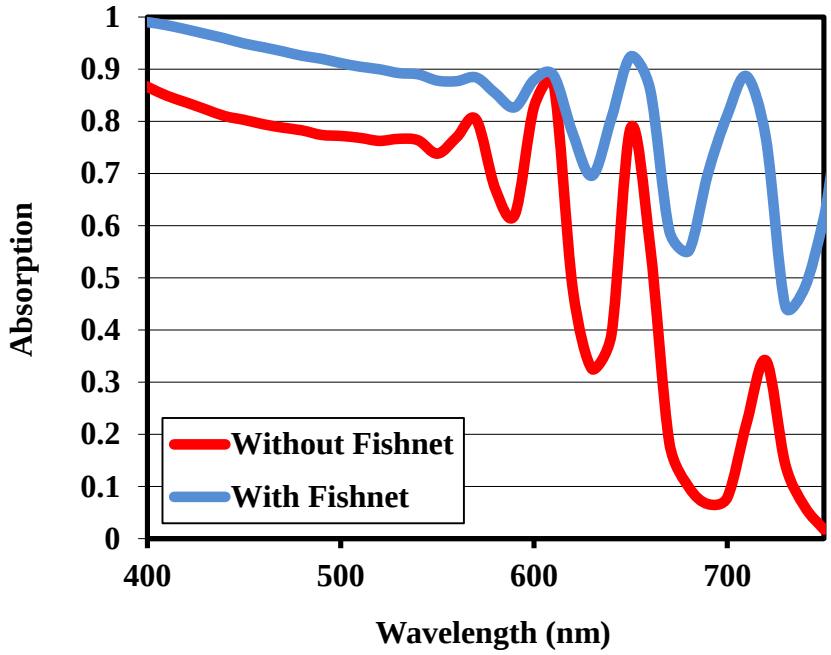

Figure 4.9: Comparison of total absorption with and without fishnet

Based on the absorption measurements, the short circuit current density J_{SC} was computed using Equation (4.2) and the results are presented in Table 4.3. The J_{SC} is enhanced by 30% as a result of including the fishnet in the back spacer.

$$J_{SC} = \int_{\lambda} eA(\lambda)\Phi_0(\lambda)d\lambda$$

Where,

e = Electronic charge

A = Absorption in the a-Si layer

Φ = Number of incident photons per wavelength

S. No.	TFSC	J_{sc}(mA/cm^2)
1.	**Without fishnet**	**11.751**
2.	**With Fishnet 01**	**15.6553**
3.	**With Fishnet 02**	**15.6775**
4.	**With Fishnet 03**	**14.9136**
5.	**With Fishnet 04**	**14.9464**

Table 4.3: J_{SC} comparison with and without the fishnet structure

Four identical Fishnet TFSC's were fabricated to test the repeatability of the results obtained above. Figure 4.10shows the absorption spectra of four Fishnet TFSC's—Fishnet01, Fishnet02, Fishnet03, and Fishnet 04. We observe almost identical patterns both with respect to magnitude as well as in the positions at which the peaks occur. This provides confirmation of two facts (i) the fabrication recipe is repeatable, and (ii) The reflection measurement is accurate.

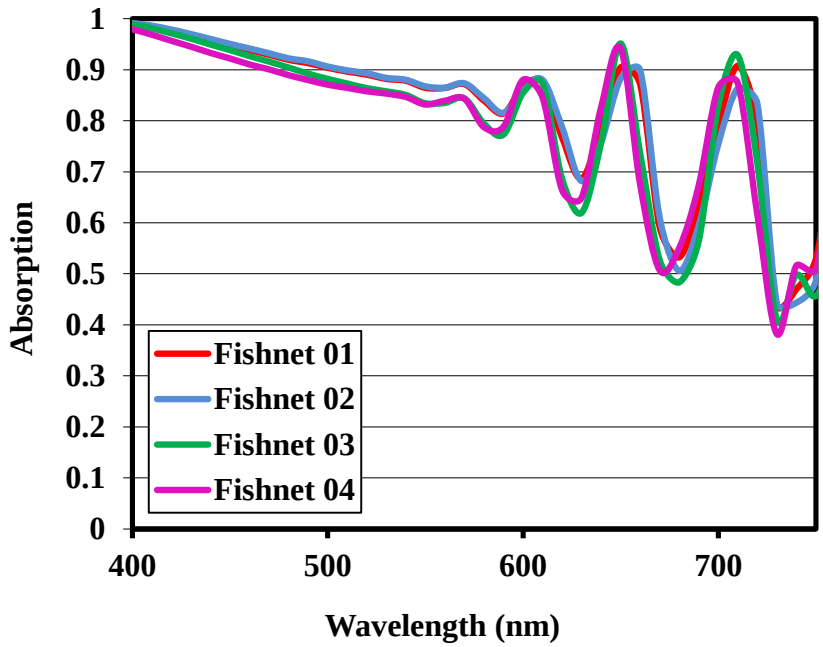

Figure 4.10: Consistent results for measurements taken for four different samples

The measurement of reflection was done for three different states of polarization. The absorption spectra corresponding to the three polarization states are shown in Figure 4.11. We observe that the spectra correlate very well for all three polarizations. We can thus infer that the performance of the Fishnet is independent of the state of polarization of the incident light.

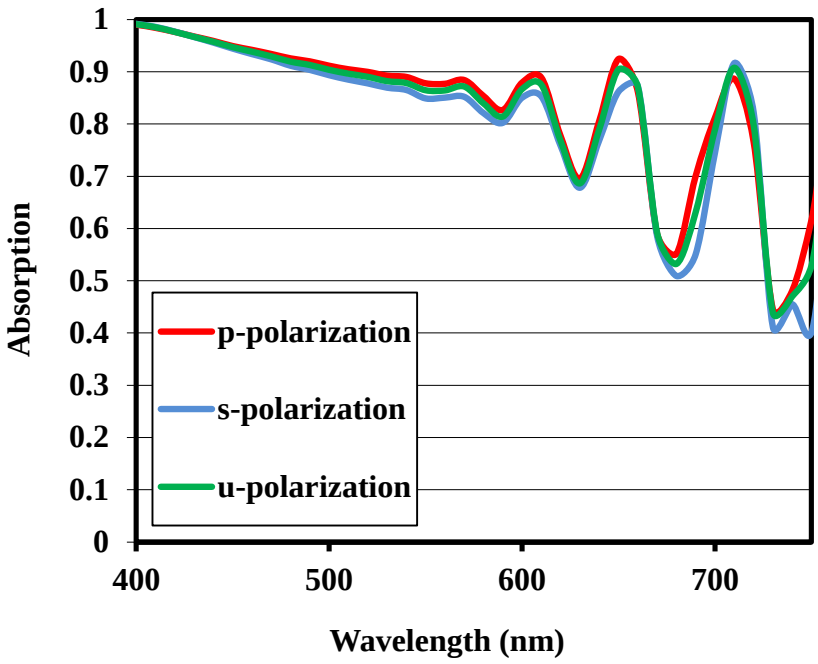

Figure 4.11: Measurements consistent for different polarization states

So far we have established that the Fishnet TFSC is successful in enhancing absorption in the cell, hence doing exactly what it was designed to do. Figure 4.12 shows the comparison of results obtained from numerical simulation versus the results obtained experimentally, both for the case with and without the fishnet.

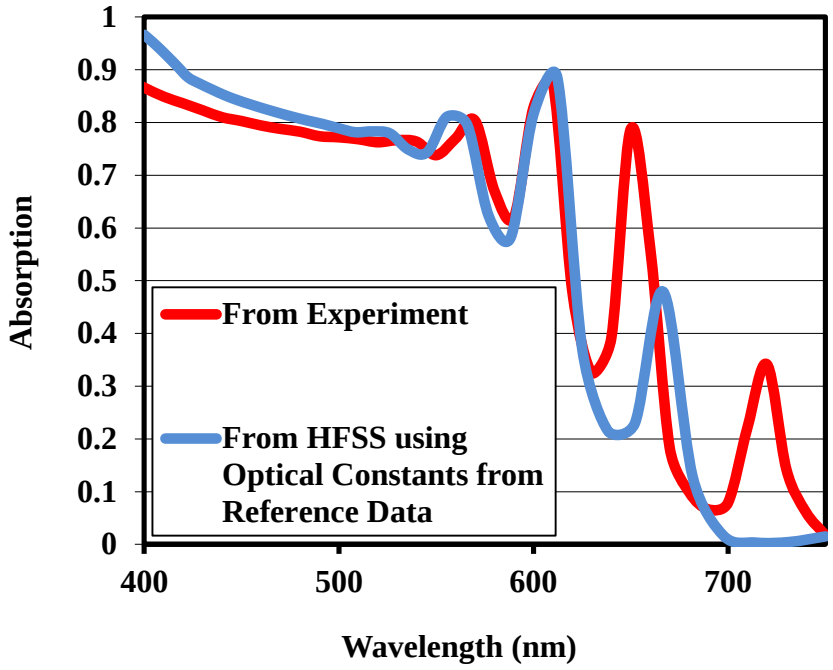

(a) Without fishnet

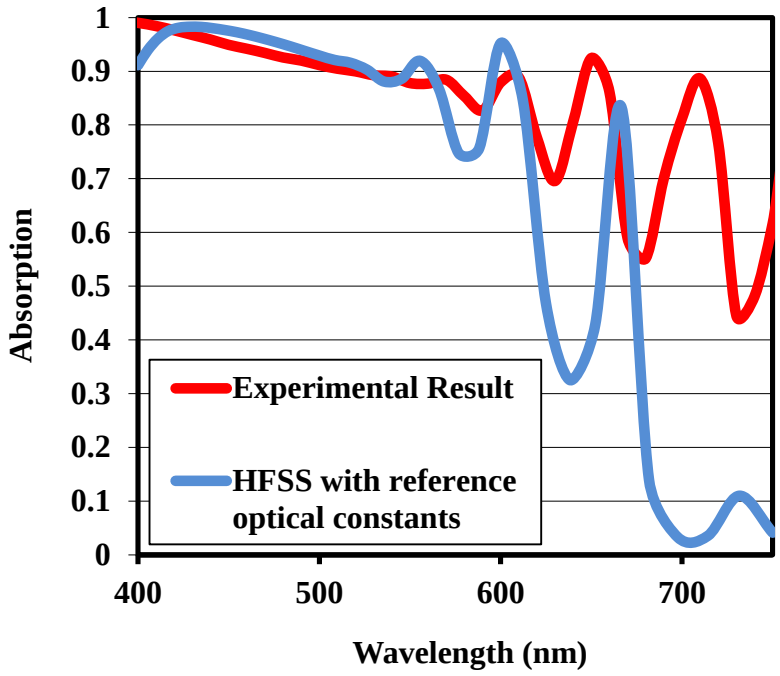

(b) With fishnet

Figure 4.12: Comparison between numerical simulation and experimental results

As we can observe, none of the plots show a good correlation between theory and experiment. This was a worrying sign and meant that we exercised very little control over how the fishnet structure actually behaved. Even though the end result was achieved, the disparity between theory and experiment left a lot to be desired. The next part of this chapter gives a detailed account of the steps taken to address these disparities.

4.4 Ellipsometric Characterization and Structural Modification of Numerical Model

The fabricated Fishnet TFSC showed an increase in the absorption as predicted by numerical simulations: but the disparity between the absorption spectrum of the experimental and simulated results could not be ignored. This essentially meant that we had no control over how the structure behaved, and that we could not engineer these structures to perform exactly as we wanted. Hence the obvious next step was to investigate the reason behind this deviation.

There could be two major reasons for the disparity observed between theory and experiment

1) The optical properties of the materials used to fabricate the Fishnet TFSC are not exactly similar to the values used for numerical simulations in HFSS. The optical constants used in HFSS simulations were taken from the database of SopraInc, and the optical constants for AZO were taken from the Materion Company. The optical constants of materials are not universally constant entities. They differ considerably depending on method of manufacture, level of purity, quality of raw materials used, etc. Hence the optical response of an experimental sample should logically be different from a theoretical model based on optical constants derived from literature.

2) In the theoretical model, the interfaces of the different layers in the Fishnet TFSC are assumed to be perfectly flat. However, that is never the case in reality. The surface roughness associated with the interfaces can potentially contribute to a significant amount of scattering. In this light we would like to stress on one particular instance of surface non-uniformity. The AZO layer deposited on top of the 27 nm Fishnet is only 50 nm thick. Quite obviously this is not going to be a flat surface, but a bumpy one. Hence we can see more scattering within the a-Si layer as a result of this non-uniformity.

4.4.1 Effects of using Ellipsometry-determined Optical Constants in the Numerical Model

As a first step we had to characterize the different materials used to fabricate the Fishnet TFSC, namely, silver, Al-doped zinc oxide, amorphous silicon and chromium. Note that chromium was used as an adhesion layer below the silver fishnet, but the original theoretical model did not take this into account. A 7 nm thick chromium fishnet was created below the silver fishnet in the new model.

The optical constants that were extracted were as close as possible to the fabricated TFSC. The results of this characterization were compared with reference values from literature and are illustrated in Figure 4.13 through Figure 4.17. First, the substrate was characterized.

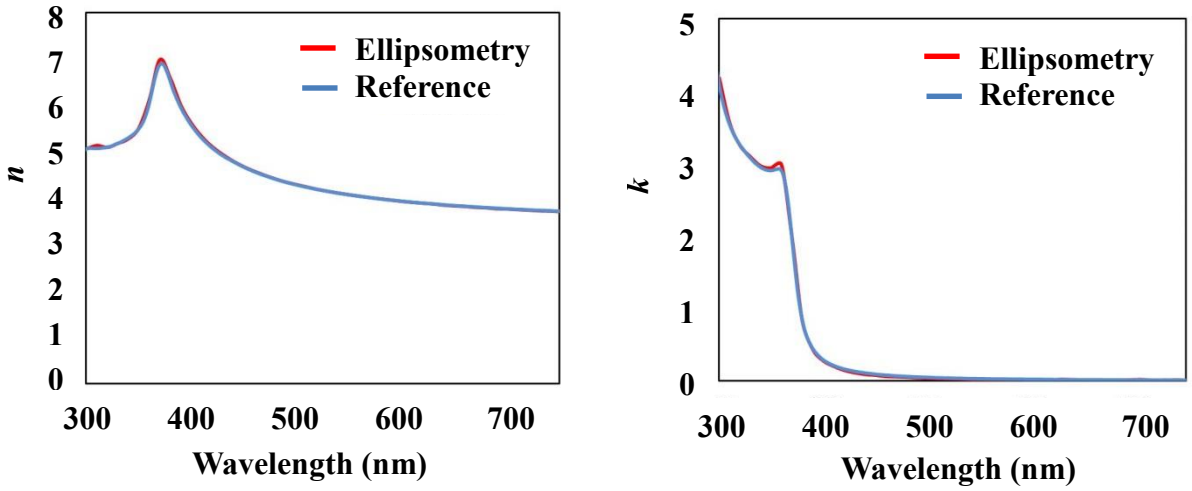

Figure 4.13: Silicon substrate

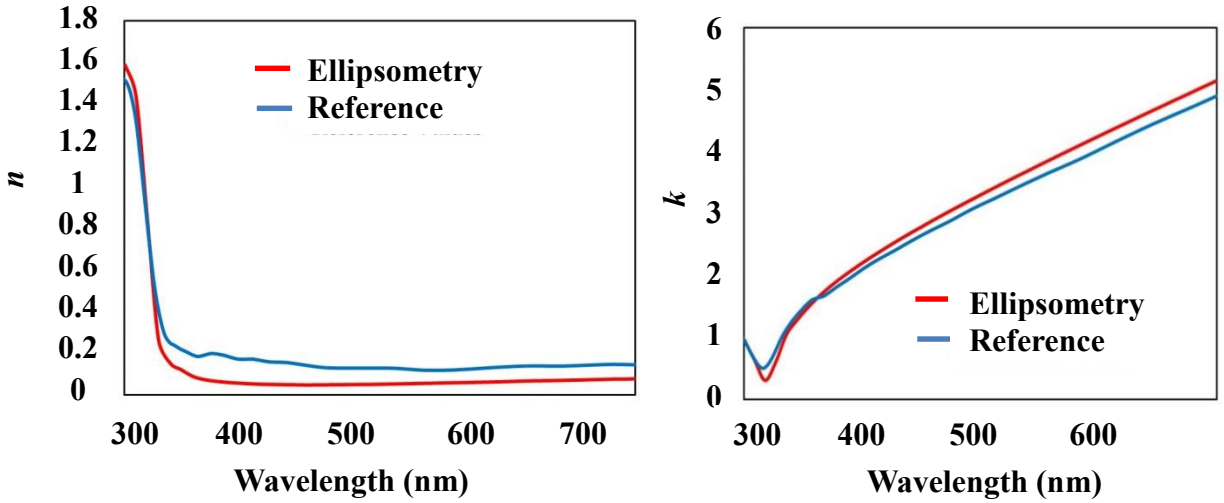

Figure 4.14: 100 nm film of silver on silicon substrate

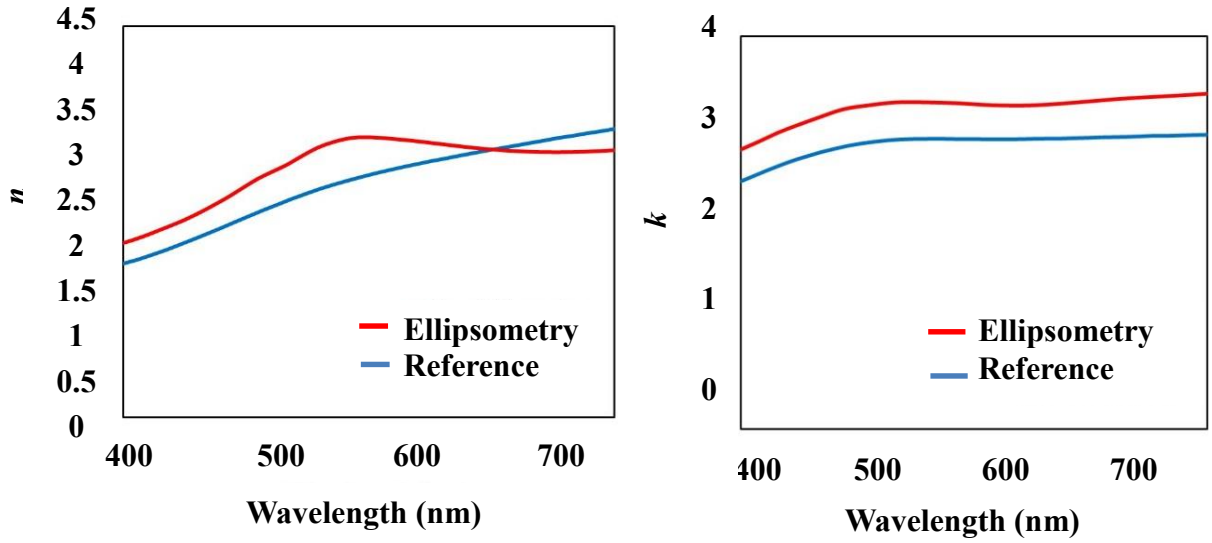

Figure 4.15: 100 nm chromium film on silicon substrate

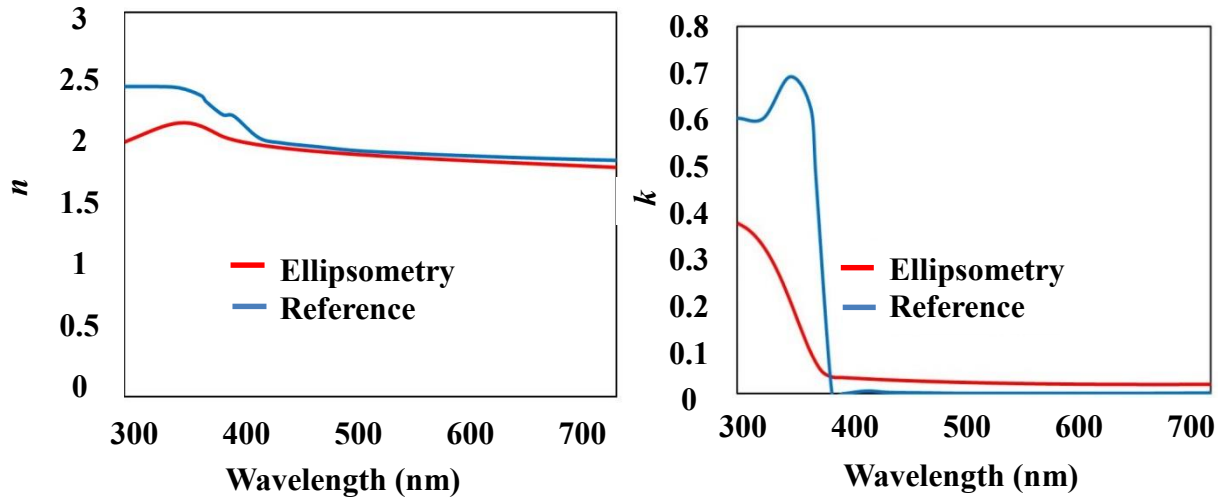

Figure 4.16: 20 nm AZO on silicon substrate

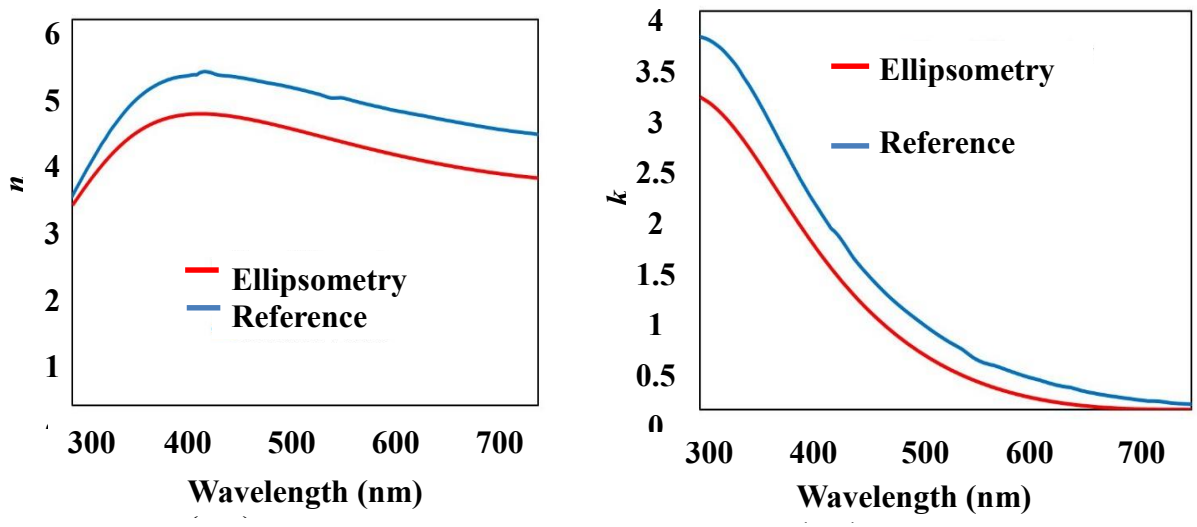

Figure 4.17 : 500 nm a-Si on silicon substrate

As we can observe the trend of variation of the optical constants is similar to the reference data, but the magnitude is quite different. The optical constants determined from ellipsometry were used as input variables in the theoretical model constructed in the HFSS software. The structure was re-simulated across a wavelength range from 400 nm to 750 nm. The absorption spectrum was plotted and compared with the case in which reference optical constants were used. The results are presented in Figure 4.18.

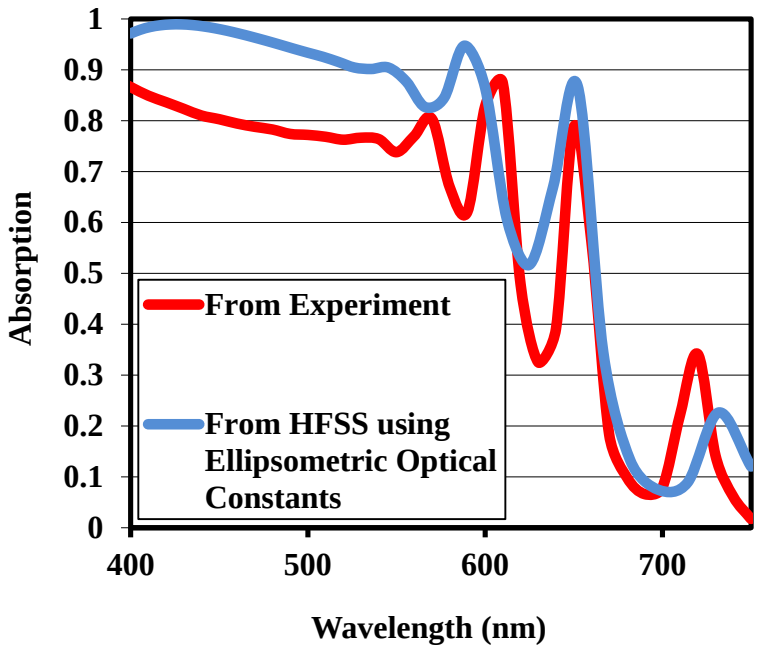

(a) Without fishnet

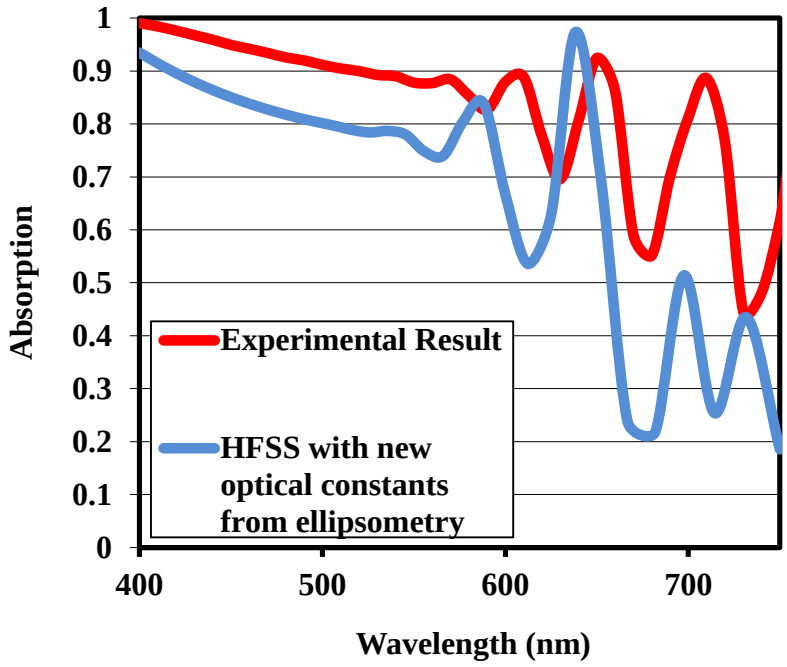

(b) With fishnet

Figure 4.18: Effect of numerical simulation using optical constants determined from ellipsometry

First, let us consider the case without the fishnet, i.e., a simple planar thin film solar cell [Figure 4.14 (a)]. It was observed that using ellipsometric optical constants improved the correlation between theory and experiment to a great extent. Using reference optical constants instead causes the theoretically predicted absorption spectrum to deviate considerably from experimental results.

With the fishnet in place, the absorption spectra using ellipsometric optical constants do a better job of replicating the experimental data, but there is still significant disparity between theory and experiment as far as the magnitude of absorption was concerned. This is the case for both the 100 nm line width sample as well as the 150 nm line width sample. What was encouraging was that the frequencies at which the maxima and minima in absorption occurred matched up. This gives enough reason to suspect that if there are bumps and roughness associated with the interfaces, the scattering (and consequently absorption) will be enhanced. This will result in an even better match between theoretical and experimental results.

4.4.2 Structural Modifications in the Numerical Model

The first step in this exercise was to determine the source of surface non-uniformities that could be responsible for enhancing the scattering. The major surface feature contributing to surface irregularity is the fishnet itself. The silver fishnet, along with the chromium adhesion layer below it, is 27 nm thick. Above this structure we deposit 50 nm AZO to enclose the fishnet within the AZO back spacer. In the theoretical model in HFSS, the second AZO layer forms a perfectly flat interface with the a-Si layer above. In reality, however, this is not the case.

When AZO is deposited over the fishnet the areas on top of the fishnet will already have a 27 nm clearance from the bottom AZO layer. As we deposit more AZO, instead of being flat, the top AZO layer will have bumps that will be approximately 27 nm high. This concept is explained schematically in Figure 4.19 (a).

This was also verified experimentally by using Atomic Force Microscopy (AFM). The same glass substrate was used, on which 50 nm AZO was deposited. The silver Fishnet along with the chromium adhesion layer underneath was fabricated, and finally the second 50 nm AZO layer was deposited on it. This sample was scanned by AFM to measure the height of the bump on the surface of the Fishnet. The result of one such measurement is presented in Figure 4.19 (b). It was seen that there is indeed a bump on the surface that measures up to exactly 27 nm on an average.

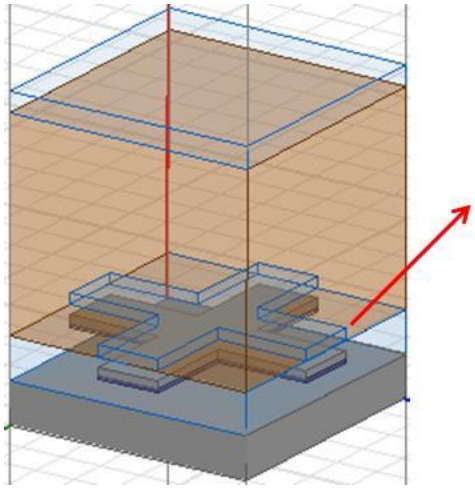

(a) Schematic of bump over fishnet

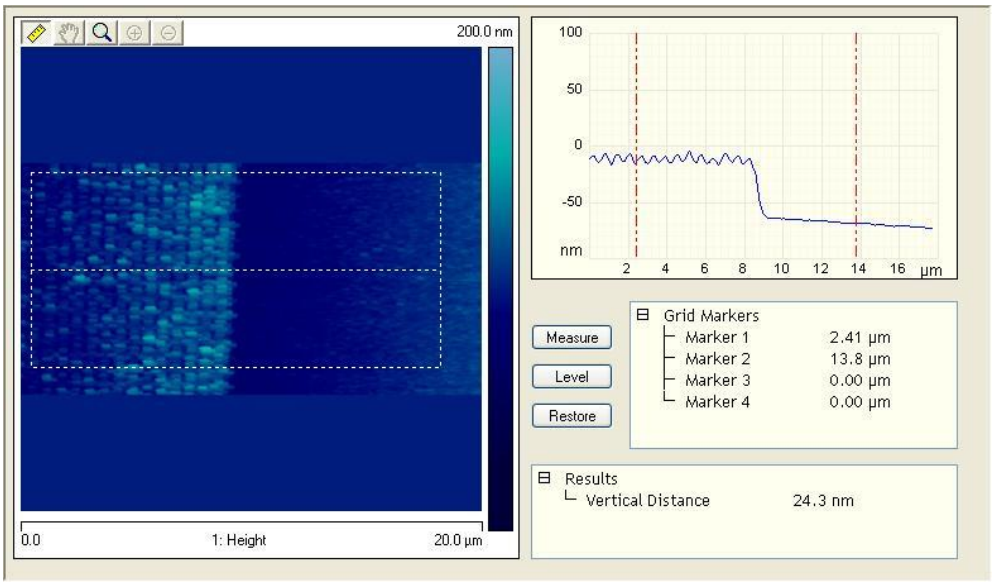

(b) Result of AFM measurements taken over the fishnet structure

Figure 4.19: Structural modification used in the numerical model

After experimental verification, the next step was to include this feature in the theoretical model and see if we can obtain a better correlation between theoretical and experimental results. An AZO fishnet was embedded within the a-Si layer, above the AZO—a-Si interface. The rest of the layers were kept the same. The result of this simulation is shown contrasted with experimental results in Figure 4.20. Compared to Figure 4.12, the results are significantly better. It can be observed that the new model comes very close to simulating the experimental results. This is by far the best matching obtained between theory and experiment. It should also be noted that the optical constants used for the new model were those determined from ellipsometry.

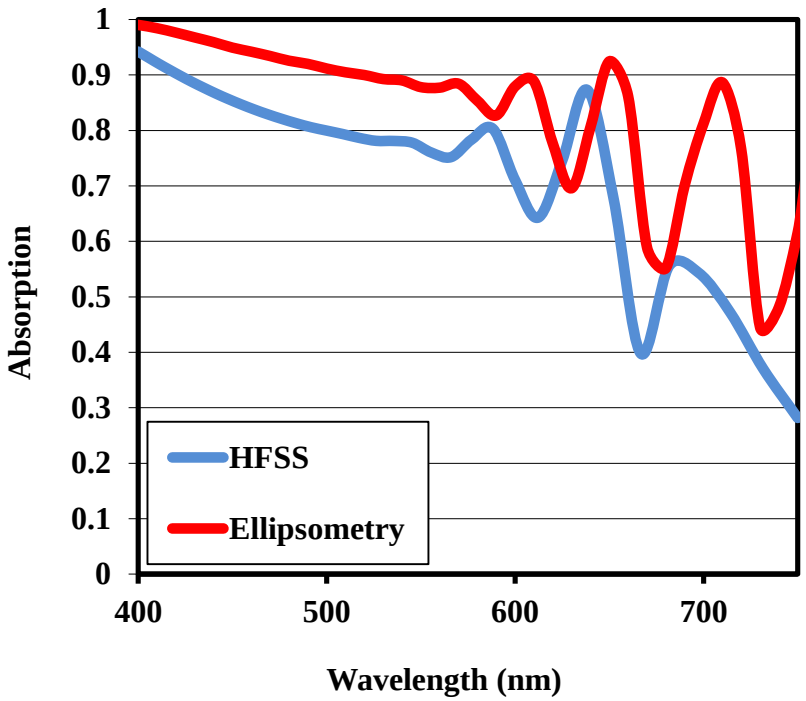

Figure 4.20: Result of including the bump on top of the fishnet in the numerical model

In this model the effect of surface roughness of the other layers was not considered. The bump was believed to have a much greater impact on the nature of the absorption spectrum as compared to minor features like surface roughness. However, including surface roughness could further help enhance the absorption in the higher wavelength region. This will produce even better correlation than what has been achieved so far. Also the angle of incidence in the numerical simulation is 0^{o}, but the ellipsometer used for the experiment can go down to only 15^{o}. This also accounts for the slight discrepancy we observe in the magnitude of absorption.

Chapter 5: Conclusions and Future Work

In this thesis it has been proved conclusively that the plasmonic fishnet structure enhances the absorption in thin film solar cells. The fishnet structure was made of silver, had a line width of 100 nm, pitch size of 600 nm, and a thickness of 20 nm. This design was tailored to produce a plasmonic resonance at 680 nm, corresponding to the band gap of amorphous silicon. The motive was to boost the absorption at this wavelength, which usually shows very low absorption. There was a 13x increase in the absorption at the resonance frequency of 680 nm as a result of including the fishnet in the back spacer layer of the solar cell. Moreover, it was proved that 83% of this absorption occurs in the amorphous silicon layer. This translated to a 30% increase in the calculated short circuit current density.

An accurate numerical model was also constructed that can be used to precisely monitor he behavior of the fishnet structure. The significance of including the surface morphology of the fishnet and the use of accurate optical constants has been illustrated. This is an important step toward improving the efficiency of the thin film solar cells to enable them to compete better with conventional wafer cells which dominate the world market today. The importance of developing low cost high efficiency thin film solar cells as a means of cheap sustainable energy cannot be stressed enough.

The future work in this project has two tracks. On the one hand, work is in progress to fabricate a solar cell device. We are collaborating with Dr. Vikram Dalal's group at the Iowa State University to deposit a p-i-n structure. Secondly, efforts are under way to fabricate a fishnet structure using Shape Memory Alloy materials like alloys of nickel an titanium. SMA materials can be trained to change shape when subject to thermal stress, only to change back to its original

form once the applied stress has been removed. Since the plasmonic resonance frequency of the fishnet depends on the geometry, it is possible to shift the resonance in our favor by using SMA materials. One application of this concept would be to counteract the temperature induced degradation in performance of solar cells. With increasing temperature, the SMA fishnet could change dimensions and provide a resonance at the frequencies that are worst affected, only to resume normal operation once the temperatures drop. Once these concepts have been illustrated on test samples, the fabrication of plasmonic patterns like the fishnet can be scaled up to meet the needs of the industry. Nanoimprinting techniques have been developed that can be used to print these patterns as part of an assembly line or roll to roll manufacture techniques [75].

References

[1] http://www.economist.com/blogs/graphicdetail/2012/12/daily-chart-19

[2] http://keithhennessey.com/2012/03/12/nearly-doubling-renewable-energy-generation/

[3] Mints, P. and Donnelly, J., "Photovoltaic Manufacturer Shipments, Capacity and Competitive Analysis 2010/2011," Navigant Solar Services Program. Palo Alto, CA, 2011.

[4] Goodrich, A., James, T. and Woodhouse, M., "Solar PV Manufacturing Cost Analysis: U.S. Competitiveness in a Global Industry," available on NREL website: http://www.nrel.gov/docs/fy12osti/53938.pdf

[5] A. Shah, P. Torres, R. Tscharner, N. Wyrsch and H. Keppner, "Photovoltaic Technology: The Case for Thin-Film Solar Cells", 30 July, 1999, Vol 285, Science.

[6] Kannan Ramanathan, Miguel A. Contreras, Craig L. Perkins, Sally Asher, Falah S. Hasoon, James Keane, David Young, Manuel Romero, Wyatt Metzger, Rommel Noufi, James Ward and Anna Duda, "Properties of 19.2% Efficiency ZnO/CdS/CuInGaSe2 Thin-film Solar Cells", Prog. Photovolt: Res. Appl. 2003; 11:225–230 (DOI: 10.1002/pip.494).

[7] Philip Jackson, Dimitrios Hariskos, Erwin Lotter, Stefan Paetel, Roland Wuerz, Richard Menner, Wiltraud Wischmann and Michael Powalla, "New world record efficiency for Cu(In,Ga)Se2 thin-film solar cells beyond 20%", Prog. Photovolt: Res. Appl. 2011; 19:894–897.

[8] Schmela, M., Kruitmann, A., *Photon Int.*, vol. 4, 38, 2002.

[9] NREL, Cadmium Use in Photovoltaics 2005, www.nrel.gov/cdte/perspective.html

[10] Schmela, M., *Photon Int. January issue*, vol. 1, 22–24, 2003.

[11] Yang, J. C., "Advances in amorphous silicon alloy technology—the achievement of high efficiency multijunction solar cells and modules", *Prog. Photovoltaics* 1998, *6*, 181–186.

[12] Shah, A. V.; Schade, H.; Vanecek, M.; Meier, J.; Vallat-Sauvain, E.; Wyrsch, N.; Kroll, U.; Droz, C.; Bailat, J., "Thin-film silicon solar cell technology", *Prog. Photovoltaics* 2004, *12*, 113 142.

[13] Schropp, R. E. I., Zeman, M., "Amorphous and Microcrystalline Silicon Solar Cells: Modeling, Materials, and Device Technology", Kluwer Academic Publishers: Boston, MA, 1998.

[14] D. L. Staebler, and C. R. Wronski, “Reversible conductivity changes in discharge-produced amorphous silicon,” Appl. Phys. Lett. 31(4), 292–294 (1977).

[15] A. V. Shah, H. Schade, M. Vanecek, J. Meier, E. Vallat-Sauvain, N. Wyrsch, U. Kroll, C. Droz, and J. Bailat, “Thin-film Silicon Solar Cell Technology,” Prog. Photovolt. Res. Appl. 12(23), 113–142 (2004).

[16] http://sharp-world.com/corporate/news/130614.html

[17] Green, M. A., “Thin-film solar cells: review of materials, technologies and commercial status,” *J Mater Sci: Mater Electron*, vol. 18, S15-S19, 2007

[18] Tool, C.J.J., Burgers, A.R., Manshanden, P. and Weeber, A.W., “Effect of Wafer Thickness on the Performance Of mc-Si Solar Cells,” *17th European Photovoltaic Solar Energy Conference*, Munich, 2001.

[19] Beaucarne, G., “Silicon Thin-Film Solar Cells,” *Adv. OptoElectronics*, vol. 10, 1155-1166, 2007.

[20] Fonash, S.J., “Solar cell device physics, 2nd ed.,” Academic Press, 2010.

[21] PV Education, http://www.pveducation.org/pvcdrom

[22] Yablonovitch, E., “Statistical Ray Optics,” *J. Opt. Soc. Am.*, vol. 72, no. 7, pp. 899-907, 1982.

[23] Yablonovitch, E. and Cody, G. D., “Intensity Enhancement in Textured Optical Sheets for Solar Cells,” *IEEE. Trans. Elctron Dev.*, vol. E-29, no. 2, 300-305, 1982.

[24] Liming Ji, “Plasmonic and photonic designs for light trapping in thin film solar cells”, University of Arkansas, ProQuest, UMI Dissertations Publishing, 2012. 3541937.

[25] Asahi glass company
http://www.agc.com/english/csr/environment/products/positive_seihin1.html

[26] Loffler, J., Groenen, R., Linden, J. L., van de Sanden, M. C. M, Schropp, R. E. I., “Amorphous silicon solar cells on natively textured ZnO grown by PECVD,” *Thin Solid Films*, vol. 392, 315-319, 2001.

[27] Groenen, R., Loffler, J., Sommeling, P.M., Linden, J. L., Hamers, E. A. G., Schropp, R. E. I. and van de Sanden, M.C.M., “Surface textured ZnO films for thin film solar cell applications by expanding thermal plasma CVD,” *Thin Solid Films*, vol. 392, 226-230, 2001.

[28] Zeman, M., van Swaaij, R. A. C. M. M., Metselaar, J. W. and Schropp, R. E. I., "Optical modeling of a-Si:H solar cells with rough interfaces: Effect of back contact and interface roughness," *J. Appli. Phys.*, vol. 88, no. 11, 6426-6443, 2000.

[29] J. Krč, F. Smole, and M. Topič, "Potential of light trapping in microcrystalline silicon solar cells with textured substrates," Prog. Photovolt. Res. Appl. 11(7), 429–436 (2003).

[30] O. Kluth, B. Rech, L. Houben, S. Wieder, G. Schöpe, C. Beneking, H. Wagner, A. Löffl, H.W. Schock, "Texture etched ZnO:Al coated glass substrates for silicon based thin film solar cells", "Thin Solid Films", Elsevier, Volume 351, Issues 1–2, 30 August 1999, Pages 247–253.

[31] M. Berginski, J. Hüpkes, W. Reetz, B. Rech, M. Wuttig, "The effect of front ZnO:Al surface texture and optical transparency on efficient light trapping in silicon thin-film solar cells", JAP, Volume:101 , Issue: 7 , Apr 2007, 074903 - 074903-11.

[32] J. Springer, B. Rech, W. Reetz, J. Muller, M. Vanecek, "Light trapping and optical losses in microcrystalline silicon pin solar cells deposited on surface-textured glass/ZnO substrates," Solar Energy Materials & Solar Cells 85 (2005) 1–11.

[33] J. Hupkesa, B. Recha, O. Klutha, T. Repmanna, B. Zwaygardta, J. Mullera, R. Dreseb, M. Wuttig, "Surface textured MF-sputtered ZnO films for microcrystalline silicon-based thin-film solar cells," Solar Energy Materials & Solar Cells 90 (2006) 3054–3060.

[34] Yu, Z., Raman, A. & Fan, S. Fundamental limit of nanophotonic light trapping in solar cells. Proc. Natl Acad. Sci. 107, 17491–17496 (2010).

[35] Zhu, J., Hsu, C. M., Yu, Z., Fan, S. and Cui, Y., "Nanodome Solar Cells with Efficient Light Management and Self-Cleaning," *Nano Lett.*, vol. 10, 1979-1984, 2010.

[36] Nam, W. J., Ji, L., Benanti, T. L., Varadan, V. V., Wagner, S., Wang, Q., Nemeth, W. Neidich, D., and Fonash, S. J., "Incorporation of a light and carrier collection management nanoelement array into superstrate a-Si:H solar cells," *Appl. Phys. Lett.*, vol. 99, no. 073113, 2011.

[37] Claus Heine and Rudolf H. Morf, "Submicrometer Gratings for Solar Energy Applications", Applied Optics, Vol. 34, Issue 14, pp. 2476-2482 (1995).

[38] C. Haase and H. Stiebig, "Optical Properties of Thin-film Silicon Solar Cells with Grating Couplers," Prog. Photovolt: Res. Appl. 2006; 14:629–641

[39] Lee, Y. J.; Ruby, D. S.; Peters, D. W.; McKenzie, B. B.; Hsu, J. W. P., "ZnO nanostructures as efficient antireflection layers in solar cells," *Nano Lett.* 2008, *8*, 1501–1505.

[40] Söderström, T.; Haug, F. J.; Terrazzoni-Daudrix, V.; Ballif, C. J., "Flexible micromorph tandem a-Si/μc-Si solar cells," Appl. Phys. 2008, 103, 114509.

[41] Python, M.; Vallat-Sauvain, E.; Bailat, J.; Donine, D.; Fesquet, L.; Shah, A.; Ballif, C. J., "Microcrystalline silicon solar cells: effect of substrate temperature on cracks and their role in post-oxidation," Non-Cryst. Solids. 2008, 354, 2258.

[42] Boccard, M.; Cuony, P.; Despeisse, M.; Domine, D.; Feltrin, A.; Wyrsch, N.; Ballif, C. Sol. Energy Mater. Sol. Cells 2011, 95, 195.

[43] Lohmuller, T.; Helgert, M.; Sundermann, M.; Brunner, R.; Spatz, J. P., "Biomimetic Interfaces for High-Performance Optics in the Deep-UV Light Range," *Nano Lett.* 2008, *8*, 1429–1433.

[44] Barnes, W. L.; Dereux, A.; Ebbesen, T. W., "Surface plasmon subwavelength optics," *Nature* 2003, *424*, 824–830.

[45] Barry, P. R.; Peter, P.; Stephen, R. F., "Three-Dimensional Nanoarchitectures: Designing Next-Generation Devices", *J. Appl. Phys.* 2004, *96*, 7519–7526.

[46] Catchpole, K. R.; Polman, "Plasmonic solar cells," A. *Opt. Express* 2008, *16*, 21793–21800.

[47] Derkacs, D.; Lim, S. H.; Matheu, P.; Mar, W.; Yu, E. T., "Improved performance of amorphous silicon solar cells via scattering from surface plasmon polaritons in nearby metallic nanoparticles," *Appl. Phys. Lett.* 2006, *89*, No. 093103.

[48] Pillai, S.; Catchpole, K. R.; Trupke, T.; Green, M. A., "Surface plasmon enhanced silicon solar cells," *J. Appl. Phys.*2007, *101*, No. 093105.

[49] Schuller, J. A., Barnard, E. S., Cai, W. S., Jun, Y. C., White, J. S. & Brongersma, M. L. Plasmonics for extreme light concentration and manipulation. Nat. Mater. 9, 193–204 (2010).

[50] Atwater, H. A. & Polman, A. Plasmonics for improved photovoltaic devices. Nat. Mater. 9, 205–213 (2010).

[51] Nakayama, K., Tanabe, K. and Atwater, H. A., "Plasmonic nanoparticle enhanced light absorption in GaAs solar cells,"*Appl. Phys. Lett.*, vol. 93, no. 121904, 2008.

[52] Schaadt, D. M. and Yu, E. T., "Enhanced semiconductor optical absorption via surface plasmon excitation in metal nanoparticles," *Appl. Phys. Lett.*, vol. 86, no. 063106, 2005.

[53] Katherine A. Willets and Richard P. Van Duyne, "Localized Surface Plasmon Resonance Spectroscopy and Sensing", Annu. Rev. Phys. Chem. 2007.58:267-297.

[54] Alexandre G. Brolo, Reuven Gordon, Brian Leathem, and Karen L. Kavanagh, "Surface Plasmon Sensor Based on the Enhanced Light Transmission through Arrays of Nanoholes in Gold Films", Langmuir 2004, 20, 4813-4815.

[55] Maier, S. A. Plasmonics - Fundamentals and Applications, 1st ed.;
Springer: New York, 2007.

[56] William L. Barnes, Alain Dereux & Thomas W. Ebbesen, "Surface plasmon subwavelength optics", Nature, Vol 424 14, August 2003, 824-830.

[57] Otto, A. Exitation of nonradiative surface plasma waves in silver by the method of frustrated total reflection. Z. Phys.216, 398 (1968).

[58] Ditlbacher, H. *et al*. Fluorescence imaging of surface plasmon fields. *Appl. Phys. Lett.* 80, 404–406 (2002).

[59] Ritchie, R. H., Arakawa, E. T., Cowan, J. J. & Hamm, R. N. Surface-plasmon resonance effect in grating diffraction. *Phys. Rev. Lett.* 21, 1530–1533 (1968).

[60] Stefan A. Maier, Steve R. Andrews, L. Martin-Moreno, and F. J. Garcia-Vidal, "Terahertz Surface Plasmon-Polariton Propagation and Focusing on periodically Corrugated Metal Wires", PRL 97, 176805 (2006).

[61] Liming Ji and Vasundara V. Varadan, "Fishnet metastructure for efficiency enhancement of a thin film solar cell", Journal Of Applied Physics 110, 043114 (2011).

[62] Zhang, S. *et. al.*, "Near-infrared double negative metamaterials," *Opt. Express*, vol.13, 4922-4930, 2005.

[63] Valentine, J., Zhang, S., Zentgraf, T., Ulin-Avila, E., Genov, D.A., Bartal, G. and Zhang, X., "Three-dimensional optical metamaterial with a negative refractive index," *Nature*, vol. 455, 376-379, 2008.

[64] Varadan, V.V., Tellakula, Anilkumar R., "Effective properties of split-ring resonator metamaterials using measured scattering parameters: Effect of gap orientation", Journal of Applied Physics (Volume:100 , Issue: 3), Aug 2006 034910 - 034910-8.

[65] V. Varadan, L. Ji, "Optical Metastructures for Trapping Light in Thin Silicon Solar Cells", Proceedings of the 35th IEEE Photovoltaics Specialists Conference (PVSC) 2010, 001057 001059.

[66] Vivian E. Ferry, Marc A. Verschuuren, Hongbo B. T. Li, Ewold Verhagen, Robert J. Walters, Ruud E. I. Schropp, Harry A. Atwater, and Albert Polman, "Light trapping in ultrathin

plasmonic solar cells", Optics Express, Volume: 18, Issue: S2 (2010), pp. A237-A245.

[67] Vivian E. Ferry , Luke A. Sweatlock, Domenico Pacifici and Harry A. Atwater, "Plasmonic Nanostructure Design for Efficient Light Coupling into Solar Cells", *Nano Lett.*, 2008, *8* (12), pp 4391–4397.

[68] Bhattacharya, J.; Chakravarty, N.; Pattnaik,S.; Dennis Slafer,W. ; Biswas,Rana ; Dalal,V.L.; "A photonic-plasmonic structure for enhancing light absorption in thin filmsolar cells", Appl. Phys. Lett. 99, 131114 (2011); doi: 10.1063/1.3641469.

[69] C. Battaglia et al, "Nanoimprint Lithography for High-Efficiency Thin-Film Silicon Solar Cells", *Nano Lett.*, 2011, *11* (2), pp 661–665.

[70] C Min, J Li, G Veronis, JY Lee, S Fan, "Enhancement of optical absorption in thin-film organic solar cells through the excitation of plasmonic modes in metallic gratings", Applied Physics Letters (Volume:96 , Issue: 13), March 2010, 133302 - 133302-3.

[71] Ragip A. Pala, John S. Q. Liu, Edward S. Barnard, Daulet Askarov, Erik C. Garnett, Shanhui Fan & Mark L. Brongersma, "Optimization of non-periodic plasmonic light-trapping layers for thin-film solar cells", *Nature Communications*, 4, 2095 (2013).

[72] Hairen Tan, Rudi Santbergen , Arno H. M. Smets , and Miro Zeman, "Plasmonic Light Trapping in Thin-film Silicon Solar Cells with Improved Self-Assembled Silver Nanoparticles", *Nano Lett.*, 2012, *12* (8), pp 4070–4076.

[73] Hummel, R. E., "Electronic Properties of Materials, 3rd ed," Springer, 2000.

[74] Johnson, P. B. and Christy, R. W. "Optical constants of the noble metals," *Phys. Rev. B*, vol.6 4370-4379, 1972.

[75] Chia-Ching Liang, Mei-Yi Liao, Wen-Yu Chen, Tsung-Chieh Cheng, Wen-Huei Chang, and Chun-Hung Lin, "Plasmonic metallic nanostructures by direct nanoimprinting of gold nanoparticles", Optics Express, Vol. 19, Issue 5, pp. 4768-4776 (2011).

Appendix 1: License for Figure 2.1

Permission on following page.

THE ECONOMIST NEWSPAPER LIMITED LICENSE TERMS AND CONDITIONS

Nov 25, 2013

This is a License Agreement between Sayan Seal ("You") and The Economist Newspaper Limited ("The Economist Newspaper Limited") provided by Copyright Clearance Center ("CCC"). The license consists of your order details, the terms and conditions provided by The Economist Newspaper Limited, and the payment terms and conditions.

All payments must be made in full to CCC. For payment instructions, please see information listed at the bottom of this form.

License Number	3276030716744
License date	Nov 25, 2013
Licensed content publisher	The Economist Newspaper Limited
Licensed content publication	The Economist
Licensed content title	Pricing sunshine
Licensed content author	
Licensed content date	Dec 28, 2012
Volume number	
Issue number	
Pages	1
Type of Use	Thesis/Dissertation
Requestor type	Student
Portion	Charts/Graphs
Circulation	1
Format	Print and electronic
Geographic Rights	United States
Order Reference Number	
Institution name	University of Arkansas
Course name	Electrical Engineering
Name of instructor	Vasundara V. Varadan
Billing Type	Invoice
Billing address	707 W Treadwell St #14 FAYETTEVILLE, AR 72701 United States

Economist VAT number	GB 340 4368 76
Permissions price	0.00 USD / 0.00 GBP
VAT/Local Sales Tax	0.00 USD / 0.00 GBP
Total	0.00 USD / 0.00 GBP

Terms and Conditions

TERMS AND CONDITIONS

These are terms and conditions under which The Economist Newspaper Limited ("The Economist") is willing to license the content ("Content") identified in the order form above ("Order Form") to the user named in the Order Form ("You"). It (along with the Order Form) forms a legally binding licence agreement ("Licence") between you and The Economist.

The Economist authorises You to reproduce the Content, subject to payment of the non-refundable fee set out in the Order Form and to the terms of this Licence.

The Licence permits the one-time use by You of the content either in the English language, or in translation in the language specified in the Order Form, in the work ("Work") and format specified in the Order Form. This permission, for electronic rights, shall last for the duration specified in the Order Form, and for print rights, shall allow the circulation/distribution specified there.

Separate permission must be sought in advance for any other proposed use whatsoever, including without limitation, future distributions, editions, translations or reproduction in any other medium from what is expressly authorised in this Licence.

Where a translation is authorised in the Order Form, You must ensure that the translation of the Content will be carried out to the highest possible standards; that it will be accurate, unabridged and without additions; and that it will not change the content, meaning, spirit or tone of the original material nor any opinion or view expressed directly or indirectly in it. The text of any Content shall not be added to or amended without the prior consent of The Publisher. Articles cannot be abridged. You accept and agree that The Economist shall not bear any liability whatsoever arising in relation to any such translated, amended or abridged material and You agree to indemnify The Economist and its affiliates against any liabilities, costs, losses or damages they may suffer in relation to any such material.

The permissions granted in this Licence are granted on a fully non-exclusive basis and The Economist may allow other users and/or publishers anywhere in the world to reproduce the same material. The Content is provided without any warranties in respect of its content or form, and to the fullest extent possible under the law, The Economist disclaims all implied warranties. The Economist shall not be liable for any costs, damages or losses arising directly or indirectly from the use of, or reliance on, the Content. The Economist's maximum aggregate liability shall in any event be limited to the amount of the fee paid by You.

The Content is the property of The Economist and is protected by copyright and other intellectual property rights. All orders that You make for any Content are subject to approval by The Economist, and The Economist has the right to deny any order.

Other than the rights specifically granted in this Licence, You may not modify, edit, copy, store, archive, distribute, transmit, create derivative works from or in any way commercially exploit the Content, or any content of The Economist, without its written permission. Except as specifically permitted in the Order Form, You may not use the Content (i) in connection with any online versions of newspapers, magazines or books; or (ii) in print or electronic (e.g., banner) advertisements.

You may not use the Content in any manner or context which would render it, or otherwise affiliate it with material that is likely to be considered (A) libellous, defamatory, inaccurate, abusive, inappropriate, profane, obscene, indecent, pornographic, sexually explicit or illegal, (B) unlawful or violating or encouraging the violation of any local, state, national or international law; (C) infringing any patent, trademark, trade secret, copyright or other proprietary rights of any party; or (D) containing expressions of bigotry, racism or hate.

You further agree not to use the Content in any manner or context that would be derogatory to the author of the Content, any publications of The Economist Newspaper Limited, or any person depicted in the Content.

You agree to abide by all copyright notices and restrictions attached to the Content and not to alter or remove any trademark, copyright or any other notice from copies of the Content.

The permissions granted under this Licence do not include the right to use any logos or trade marks of The Economist and acknowledgement in the following form must be given in each place where the Content is reproduced:

"© The Economist Newspaper Limited, London (issue date)".

You acknowledge that that The Economist does not usually own the copyright in any photographs, cartoons or drawings. Permission to reproduce any of these is not given to You and would in any case probably also need to be obtained directly from the individual copyright holders. You agree fully to indemnify The Economist against any liabilities, costs, losses or damages The Economist may suffer arising out of or in relation to Your use of any photographs, cartoons or drawings.

This Licence is for Your benefit only (as the user named on the Order Form) and Your rights or obligations may not be assigned, transferred or sublicensed by You. The Economist is entitled to terminate and revoke this Licence with immediate effect if You breach any of its terms.

The Economist Newspaper Limited or CCC may, within ten (10) days from the date of license, deny the permissions described in this License at their sole discretion, for any reason or no reason, with a full refund payable to you (where permission is denied for reasons other than your misconduct or breach). Notice of such denial will be made using the contact information provided by you. Failure to receive such notice will not alter or invalidate the denial. In no event will or CCC be responsible or liable for any costs, expenses or damage incurred by you as a result of a denial of your permission request, other than a refund of the amount(s) paid by you to CCC for denied permissions.

License Contingent on Payment. While you may exercise the rights licensed immediately upon

issuance of the license at the end of the licensing process for the transaction, provided that you have disclosed complete and accurate details of your proposed use, no license is finally effective unless and until full payment is received from you (either by publisher or by CCC) as provided in CCC's Billing and Payment terms and conditions. If full payment is not received on a timely basis, then any license preliminarily granted shall be deemed automatically revoked and shall be void as if never granted. Further, in the event that you breach any of these terms and conditions or any of CCC's Billing and Payment terms and conditions, the license is automatically revoked and shall be void as if never granted. Use of materials as described in a revoked license, as well as any use of the materials beyond the scope of an unrevoked license, may constitute copyright infringement and publisher reserves the right to make any and all action to protect its copyright in the materials

This Licence shall be governed by English law and You submit to the exclusive jurisdiction of the English courts.

Special Terms: None

v1.2

If you would like to pay for this license now, please remit this license along with your payment made payable to "COPYRIGHT CLEARANCE CENTER" otherwise you will be invoiced within 48 hours of the license date. Payment should be in the form of a check or money order referencing your account number and this invoice number RLNK501167446. Once you receive your invoice for this order, you may pay your invoice by credit card. Please follow instructions provided at that time.

Make Payment To:
Copyright Clearance Center
Dept 001
P.O. Box 843006
Boston, MA 02284-3006

For suggestions or comments regarding this order, contact RightsLink Customer Support: customercare@copyright.com or +1-877-622-5543 (toll free in the US) or +1-978-646-2777.

Gratis licenses (referencing $0 in the Total field) are free. Please retain this printable license for your reference. No payment is required.